

This is a postprint version of the following published document:

Santos, T. dos; N'souglo, K.E.; Rodríguez-Martínez, J.A. Dynamic spherical cavity expansion in Gurson materials with uniform and non-uniform distributions of porosity, in: *Mechanics of Materials*, Vol. 134, July 2019, Pp. 115-131

DOI: <https://doi.org/10.1016/j.mechmat.2019.04.017>

© 2019 Elsevier Ltd. All rights reserved



This work is licensed under a [Creative Commons Attribution-NonCommercial-NoDerivatives 4.0 International License](https://creativecommons.org/licenses/by-nc-nd/4.0/).

Dynamic spherical cavity expansion in Gurson materials with uniform and non-uniform distributions of porosity

T. dos Santos^a, K. E. N'souglo^b, J. A. Rodríguez-Martínez^{b,*}

^a*Departamento de Engenharia Mecânica, Universidade Federal de Santa Maria, Av. Roraima, 1000, Prédio 7, Santa Maria, RS, 97105-900, Brazil.*

^b*Department of Continuum Mechanics and Structural Analysis, University Carlos III of Madrid, Avda. de la Universidad, 30, 28911 Leganés, Madrid, Spain*

Abstract

This paper investigates both theoretically and using finite elements the elastoplastic field induced by a pressurized spherical cavity expanding dynamically in an infinite medium modelled using the Gurson-Tvergaard-Needleman porous plasticity approach. The theoretical model, which assumes that the porosity is uniformly distributed in the material and the cavitation fields are self-similar, incorporates artificial viscous stresses into the original formulation of Cohen and Durban (2013b) to capture the shock waves that emerge at high cavitation velocities. The finite element calculations, performed in ABAQUS/Explicit (2013) using the Arbitrary Lagrangian Eulerian adaptive meshing available in the code, simulate the cavity expansion process in materials with uniform and non-uniform distributions of porosity. The finite element results show that the distribution of porosity has small influence on the cavitation velocity, as well as on the location of the shock wave, which are primarily determined by the cavity pressure and the average material properties. In contrast, it is shown that the intensity of the shock wave, evaluated based on the maximum value of the plastic strain rate within the shock, depends on the local material porosity. The ability of the theoretical model to reproduce the numerical results obtained for the various distributions of porosity used in this work is exposed and discussed.

Keywords: Dynamic spherical cavitation, Shock waves, Gurson materials, Porosity distribution, Finite elements

1. Introduction

The work of Hopkins (1960) was among the first studies to investigate the problem of a spherical cavity expanding dynamically in an elastoplastic medium. A few years later, the model of Hopkins (1960) was used by Goodier (1965) to analyse the penetration of spherical projectiles into metal targets. While in recent years alternative theoretical approaches to study the problem of a projectile penetrating a metallic target have been developed (e.g. Yarin et al. (1995); Roisman et al. (1997); Rubin et al. (2016)), it is still widely accepted that spherical cavitation models are very useful in understanding the mechanics of penetration (Cohen and Durban,

*Corresponding author. E-mail address: jarmarti@ing.uc3m.es

2013a). An important reason for this is that, as stated by Durban and Masri (2004), spherical cavitation models provide *fairly simple, yet accurate, expressions for key parameters like the resisting force and penetration depth*.

Thus, following the work of Goodier (1965), several authors have contributed over the last decades to the research on dynamic spherical cavitation with application to high velocity penetration problems. For instance, Forrestal et al. (1988) used cavity-expansion approximations to obtain closed-form penetration equations for elastic-perfectly plastic targets (Forrestal and Luk, 1988). The authors obtained predictions for penetration depths that were in *reasonable agreement* with experimental data obtained from tests in which maraging steel rods with spherical, ogival, and conical noses were impacted onto 6061-T651 aluminum targets at velocities ranging from 0.4 to 1.4 km/s. Shortly after, Forrestal et al. (1991), following the work of Luk et al. (1991), included the strain hardening of the target material in their analytical model. As in their previous work, the theoretical predictions were compared to experimental data obtained from high-velocity impact tests in which projectiles with different geometries were used to penetrate 6061-T651 aluminum targets, and satisfactory agreement between theory and experiments was obtained. In Forrestal et al. (1995), the authors compared their analytical models for incompressible and compressible elastic-perfectly plastic constitutive idealizations to numerical simulations performed by Hallquist (1990), McGlaun et al. (1990) and Chen (1995). The predictions of the analytical models, obtained assuming different friction coefficients between projectile and target, were in good agreement with the numerical results. Warren and Forrestal (1998) extended previous penetration models published by Forrestal et al. (1988, 1991, 1995) by including the strain rate sensitivity in the constitutive model of the target material. The theoretical results were compared with experiments previously published by the authors for 6061-T651 aluminum targets, and the influence of material rate sensitivity in the depth of penetration was brought to light. Some years later, Forrestal and Warren (2008) used the penetration model published in Forrestal et al. (1988, 1992) to identify the range of penetration velocities for which target inertia plays a role in the penetration depth of 6061-T651 aluminum targets impacted by ogive-nose projectiles. In this respect, the recent work of Warren (2016) showed that target inertia effects also depend on projectile geometry and nose shape, projectile density and target material properties.

However, in the last fifteen years, the researchers who worked most actively in the development of analytical penetration models based on dynamic spherical cavity expansion equations were Durban and co-workers (Durban and Masri, 2004; Masri and Durban, 2005; Cohen et al., 2010; Cohen and Durban, 2013b). Namely, Durban and Masri (2004) studied dynamic spherical cavitation fields in pressure sensitive elastoplastic materials modelled with Drucker-Prager plasticity. The results presented by the authors revealed that the cavitation pressure increases when the elastic compressibility decreases and the plastic compressibility increases. Masri and Durban (2005) derived a power expansion solution for the problem of a spherical cavity expanding dynamically in a compressible von Mises solid. Note that this analytical study covered only the case where the cavity expansion velocity was

much smaller than the speed of sound in the solid. The authors considered both elastic/perfectly plastic response and strain-hardening behaviour, and applied their analytical model to predict the penetration depths obtained in the experiments of Forrestal et al. (1988, 1991). Good agreement between experiments and analytical predictions was reported. Few years later, Cohen et al. (2010) found out that, for cavity expansion velocities greater than those investigated by Masri and Durban (2005), plastic shock waves emerge in the material. The shocks, which led to discontinuities in the field variables, were modelled imposing jump (Hugoniot) conditions regarding mass and momentum conservation at the wave front. It was shown that the level of discontinuities induced by the shock increases with the cavitation velocity. The work of Cohen et al. (2010) was continued by Cohen and Durban (2013b) who investigated hypervelocity spherical cavitation fields in porous elastoplastic solids described with the Gurson model. Cohen and Durban (2013b) showed that material porosity favours the development of shock waves. The authors also showed that in the spherical cavity expansion problem, for a given cavity expansion velocity, the level of discontinuities induced by the shock increases with the material porosity.

A key hypothesis in the analytical works of Durban and co-workers (Durban and Masri, 2004; Masri and Durban, 2005; Cohen et al., 2010; Cohen and Durban, 2013b) is the self-similarity of the cavitation fields. This hypothesis was verified by Rodríguez-Martínez et al. (2014) with finite element simulations performed using ABAQUS/Explicit (2013) for elastoplastic materials modelled with von Mises plasticity and different strain hardening behaviours. The numerical simulations of Rodríguez-Martínez et al. (2014) also showed that shock waves emerge at high cavitation velocities, in agreement with the analytical predictions of Cohen et al. (2010). However, unlike in the theoretical model, the shock wave in the finite element calculations did not entail a finite jump in field variables. The authors noticed that, due to the artificial viscosity included by ABAQUS/Explicit (2013), the shock wave in the finite element calculations was described as a thin band of steep gradients of stress, strain, density, velocity and increased strain rates.

Motivated by these results, in the present paper we incorporate artificial viscous stresses into the theoretical model of Cohen and Durban (2013b) to capture the shock waves that emerge at high cavitation velocities in porous elastoplastic materials modelled using Gurson plasticity. Our approach, which is based on the works of Wilkins (1980) and Lew et al. (2001), leads to *smooth solutions* of the set of differential equations which govern the problem, so that it is not necessary to use the Hugoniot conditions for the calculation of the shock. The results obtained from our theoretical model are validated with finite element simulations performed in ABAQUS/Explicit (2013). A good agreement between theoretical and numerical predictions is obtained in terms of cavitation velocity, stress and density fields, and shock wave location. The finite element calculations also show that the steady-state expansion of the cavity is reached in few microseconds (for the highest cavitation velocity considered), thus verifying the assumption of steady cavitation fields used in the theoretical model. In addition to the finite element simulations used to validate the theoretical model (which assumes that the initial porosity is uniformly

distributed in the material), we have performed numerical calculations with non-uniform distributions of initial porosity that aim at idealizing the micro-structure of metallic materials with inclusions and second-phase particles randomly distributed in the bulk (Ohno and Hutchinson, 1984; Becker, 1987; Huang, 1993; Bilger et al., 2007). These numerical calculations show that the distribution of porosity has small influence on the cavitation velocity, as well as on the location of the shock wave, which are primarily determined by the average material properties. In contrast, it is shown that the intensity of the shock wave strongly depends on the local porosity at the shock location.

2. Constitutive framework

The mechanical behaviour of the material is described using the Gurson-Tvergaard-Needleman (GTN) constitutive model (Gurson, 1977; Tvergaard, 1981, 1982) pre-implemented in ABAQUS/Explicit (2013). For the sake of clarity, the main features of the model are briefly presented in this section.

The flow potential has the form:

$$\Phi = \left(\frac{\sigma_e}{\sigma_y} \right)^2 + 2q_1 f \cosh \left(\frac{3q_2 \sigma_h}{2\sigma_y} \right) - 1 - (q_1 f)^2 \quad (1)$$

where q_1 and q_2 are material parameters, and f is the void volume fraction. The effective von Mises stress, σ_e , and the hydrostatic pressure, σ_h , are defined by:

$$\sigma_e = \sqrt{\frac{3}{2} \mathbf{s} : \mathbf{s}}; \quad \sigma_h = \frac{1}{3} \boldsymbol{\sigma} : \mathbf{1}; \quad \mathbf{s} = \boldsymbol{\sigma} - \sigma_h \mathbf{1} \quad (2)$$

where $\boldsymbol{\sigma}$ is the macroscopic Cauchy stress tensor, \mathbf{s} is its deviatoric part, and $\mathbf{1}$ is the unit second order tensor.

Moreover, σ_y is the flow strength of the fully dense matrix material described by the following power-type relation:

$$\sigma_y = \sigma_0 \left(1 + \frac{\bar{\varepsilon}^p}{\varepsilon_0} \right)^n \quad (3)$$

being $\bar{\varepsilon}^p = \int_0^t \dot{\bar{\varepsilon}}^p(\tau) d\tau$ the effective plastic strain, where $\dot{\bar{\varepsilon}}^p$ is the effective plastic strain rate (see equation (8)). Moreover, σ_0 is the initial yield stress of the matrix material, n is the strain hardening parameter, and ε_0 is the reference strain. For the sake of simplicity, we have not considered the temperature and strain rate dependences of the flow strength of the matrix material. This, in turn, facilitates to derive a theoretical model for the spherical cavity expansion problem studied in this work, see Appendix A.

The rate of deformation tensor is taken to be the sum of an elastic part, \mathbf{d}^e , and a plastic part, \mathbf{d}^p , as follows:

$$\mathbf{d} = \mathbf{d}^e + \mathbf{d}^p \quad (4)$$

where the elastic part is related to the rate of the stress by the following hypo-elastic law:

$$\overset{\nabla}{\boldsymbol{\sigma}} = \mathbf{C} : \mathbf{d}^e = \mathbf{C} : (\mathbf{d} - \mathbf{d}^p) \quad (5)$$

with $\overset{\nabla}{\boldsymbol{\sigma}}$ being the objective stress rate (it corresponds to the Green-Naghdi derivative in ABAQUS/Explicit (2013)) and \mathbf{C} being the tensor of isotropic elastic moduli given by:

$$\mathbf{C} = \frac{E}{1+\nu} \mathbf{I}' + \frac{E}{3(1-2\nu)} \mathbf{1} \otimes \mathbf{1} \quad (6)$$

where E is the Young's modulus, ν is the Poisson's ratio and \mathbf{I}' is the unit deviatoric fourth order tensor.

The plastic part of the rate of deformation tensor follows the direction normal to the flow potential:

$$\mathbf{d}^p = \dot{\lambda} \frac{\partial \Phi}{\partial \boldsymbol{\sigma}} \quad (7)$$

where $\dot{\lambda}$ is the non-negative plastic flow proportionality factor.

The plastic part of the rate of deformation tensor and the effective plastic strain rate in the matrix material are related by enforcing equality between the rates of macroscopic and matrix plastic work:

$$\boldsymbol{\sigma} : \mathbf{d}^p = (1 - f) \sigma_y \dot{\varepsilon}^p \quad (8)$$

Moreover, assuming the incompressibility of the matrix material, the evolution of the void volume fraction is defined as:

$$\dot{f} = (1 - f) \mathbf{d}^p : \mathbf{1} \quad (9)$$

Note that void nucleation is not considered in the present analysis. Hence, if the initial void volume fraction

Symbol	Property and units	Value
ρ_0	Initial density (kg/m ³)	7600
E	Young's modulus (GPa), Eq. (6)	70
ν	Poisson's ratio, Eq. (6)	0.3
q_1	Material parameter, Eq. (1)	1.25
q_2	Material parameter, Eq. (1)	1.0
σ_0	Reference yield stress (MPa), Eq. (3)	300
n	Strain hardening exponent, Eq. (3)	0.1
ε_0	Reference strain, Eq. (3)	0.00429
f_0	Average value of initial VVF	0.001, 0.01, 0.1

Table 1: *Material parameters used in the finite element calculations (Srivastava et al., 2014; N'souglo and Rodríguez-Martínez, 2018). VVF stands for void volume fraction (porosity).*

is zero, the macroscopic material is fully dense and follows von Mises plasticity.

The flow strength of the matrix material, Eq. (3), has been used along with the GTN model pre-implemented in ABAQUS/Explicit through a user-defined subroutine VUHARD (ABAQUS/Explicit, 2013). The material parameters related to the elastic law, Eqs. (5)-(6), the flow potential, Eq. (1), and the flow strength of the matrix material, Eq. (3), taken from Srivastava et al. (2014) and N'souglo and Rodríguez-Martínez (2018), are given in Table 1. Note that the average initial void volume fraction, from now indistinctly referred to as porosity, is the average value of initial porosity over the whole sample, see section 3.1 for details.

3. Finite element model

This section describes the features of the axisymmetric finite element model developed in ABAQUS/Explicit (2013) to simulate the dynamic, spherical, cavity-expansion problem. The model is identical to the one used by Rodríguez-Martínez et al. (2014), that was based on the previous work of Rosenberg and Dekel (2008). The specimen is a sphere of very large radius $R_s = 300$ mm which has a small cavity of radius $R_c = 0.5$ mm in its center. Due to the symmetry of the model, only the $\theta \geq 0$ half of the specimen has been analyzed (see Fig. 1). The sample is initially at rest and undeformed, while a constant internal pressure p is applied at the cavity wall. The dimensions (radii) of the sphere and the cavity do not influence the simulation results. We have checked that, for all the numerical simulations, the stress waves generated by the application of the cavity pressure reach the free boundary of the sphere after the steady cavitation field has developed.

The model has been meshed with 240,000 four-node axisymmetric reduced integration elements, CAX4R in ABAQUS notation. The mesh shows radial symmetry, in order to retain the symmetry of the problem, with 200 elements along the circumferential direction and 1200 along the radial direction. The elements size is constant along the circumferential direction whereas it decreases along the radial direction as the cavity is approached.

Namely, the elements show a bias ratio of 100 along the radial direction. The dimensions of the elements located near the cavity are $12 \mu\text{m} \times 4 \mu\text{m}$. Small elements are needed to capture the large gradients of stress and strain which arise in this region of the specimen. Moreover, these large gradients of stress and strain lead to severe mesh distortion. In order to reduce this problem, the Arbitrary Lagrangian Eulerian (ALE) adaptive meshing available in ABAQUS/Explicit (2013) has been applied to the entire model. ALE adaptive meshing uses a single mesh definition that is gradually smoothed within analysis steps. The frequency of adaptive meshing is set to 1 and the remeshing sweeps per increment are set to 10. As reported by Rodríguez-Martínez et al. (2014), these values of the controlling parameters of the adaptive meshing ensure a proper aspect ratio of the elements during the simulations.

Note that ABAQUS/Explicit (2013) introduces artificial damping in the calculations in order to attenuate the numerical solution and ensure stability, see Aranda-Iglesias et al. (2017). The code generates bulk viscosity pressures, which are linear and quadratic, respectively, in the volumetric strain rate. This artificial viscosity is controlled by two parameters ϖ (linear viscosity) and χ (quadratic viscosity). Unless otherwise noted, in the calculations shown in section 5, we have used the default values of the code 0.06 and 1.2, respectively. Only in few calculations, with large initial porosity and applied pressure, we have increased the value of ϖ , see section 5.

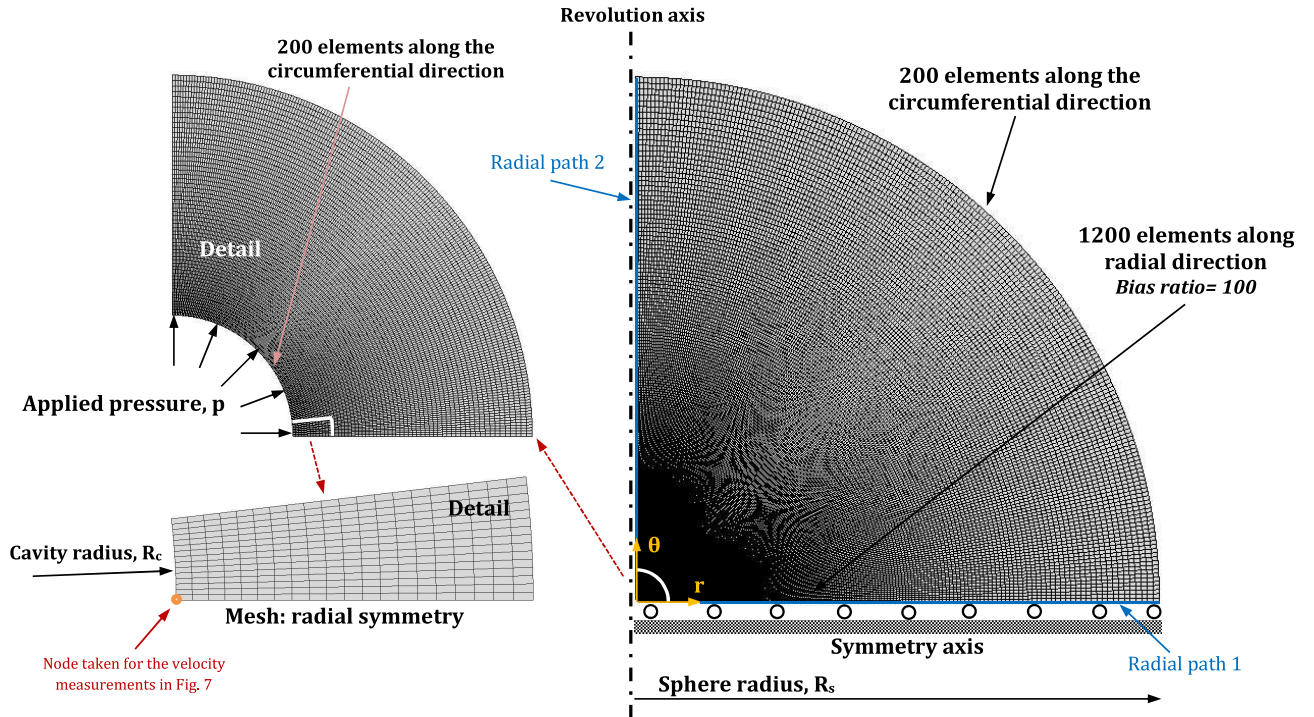


Figure 1: Axisymmetric finite element model used to analyse dynamic spherical cavity expansion. This figure is adapted from Rodríguez-Martínez et al. (2014).

3.1. Porosity distribution

The porosity in the GTN model idealizes the void nucleating particles that can be found in many metallic materials. These particles are considered sources of damage and preferential sites for the nucleation of cracks. There are many numerical works in the literature, investigating a wide variety of engineering problems, in which the initial porosity is considered uniformly distributed in the material (e.g. Zhang (1996), Vadillo et al. (2008)). However, for some materials, the void nucleating particles may be non-uniformly distributed in the bulk (e.g. Ohno and Hutchinson (1984), Becker (1987), Huang (1993), Bilger et al. (2007)). Accordingly, in this work we perform numerical simulations with specimens with uniform and non-uniform distributions of initial porosity. Three different average values of initial void volume fraction f_0 are used in the calculations reported in section 5, namely 0.001, 0.01 and 0.1 (see Table 1).

The specimens with uniform distribution of porosity are modelled assigning the same value of f_0 to all the nodes of the mesh. The specimens with non-uniform distribution of porosity are modelled using the methodology developed by N'souglo and Rodríguez-Martínez (2018). Namely, the average value of the initial porosity in the sample f_0 is obtained assigning finite (positive) values of initial porosity only to some nodes (and zero to the others). The percentage of nodes, over the total number of nodes in the sample, that do have initial porosity is denoted as F . Three values of F have been investigated in the simulations: 10%, 25% and 40%. The specific nodes with positive initial porosity are selected randomly using the function *randperm* of MATLAB. Each of these nodes has allotted a random value of initial porosity that was generated using the normal distribution function *normrnd* of MATLAB. The mean and the standard deviation of this normal distribution are $\mu = f_0/F$ and $\sigma = \mu C_v$, respectively. The relative standard deviation, C_v , determines the maximum dispersion of the generated random values of porosity. Three different values of C_v have been used in the numerical simulations presented in section 5, namely 5%, 15% and 25%. Moreover, note that, for any given combination of F , C_v and f_0 , we could generate an infinite number of random porosity distributions: different nodes with positive initial porosity and different values of porosity for each one. Nevertheless, in the finite element simulations reported in section 5 we have used only one random non-uniform distribution of porosity. It is out of the scope of this paper to assess the specific effect that the randomness of the non-uniform porosity distribution has on the finite element results. Note that, due to the axisymmetry of the finite element model, the non-uniform porosity distributions are 2D microstructural idealizations (Tvergaard and Needleman, 1992, 2006). Describing more realistic microstructures require a fully 3D analysis, which is out of the scope of this paper.

4. Main features of the theoretical model

In this section we summarize the main features of the theoretical model developed to investigate dynamic spherical cavitation fields in Gurson materials. The complete formulation can be found in Appendix A. The

model used in this paper shows two differences with respect to the formulation reported in the seminal work of Cohen and Durban (2013b): (1) it includes the parameters q_1 and q_2 in the flow potential of the constitutive model, and (2) it uses the artificial viscosity approach to capture the formation of plastic shocks at high cavitation velocities. Note that solutions of rate-independent nonlinear differential equations commonly exhibit first-order discontinuities associated with shock wave propagation. Due to unbounded derivatives, this singular behaviour causes difficulties in the numerical integration of the corresponding differential equations using typical numerical schemes such as the Runge-Kutta methods. While Cohen et al. (2010) and Cohen and Durban (2013b) solved this problem imposing jump (Hugoniot) conditions regarding mass and momentum conservation at the wave front, in this paper (as previously mentioned) we use the artificial viscosity approach developed, for instance, by von Neumann and Richtmyer (1950); Landshoff (1955); Wilkins (1980) and Lew et al. (2001). This approach, which stands out for its simplicity, leads to *smooth solutions* of the set of differential equations which govern the problem, facilitating the integration process. Recall that the outputs of this theoretical model, which considers a uniform distribution of porosity in the specimen, will be compared in section 5 with the results obtained from the finite element model presented in section 3, in which uniform and non-uniform distributions of porosity are considered.

Following Cohen and Durban (2013b), the problem is modelled as a pressurized spherical cavity of instantaneous radius a expanding under self-similar, steady-state conditions in an infinite medium, see Fig. 2. Let (r, θ, ϕ) stand for the Eulerian coordinates of a material point with reference to a spherical system with the origin located at the center of the cavity denoted by O in Fig. 2. It is assumed that the only independent variable is the nondimensional radial coordinate $\xi = r/a$. In the formulation used in this paper, see Appendix A, equations (A.8), (A.9), (A.16), (A.27) and (A.29) provide a system of five differential equations with derivatives of five unknowns: dimensionless radial velocity (v), dimensionless radial elastoplastic stress (Σ_{rr}), dimensionless circumferential elastoplastic stress ($\Sigma_{\theta\theta}$), dimensionless yield stress (Σ_y) and dimensionless radial viscous stress (Σ_{rr}^v). Moreover, porosity (f), density (ρ) and dimensionless circumferential viscous stress ($\Sigma_{\theta\theta}^v$) are calculated from the algebraic relations (A.15), (A.21) and (A.28).

Integration is performed over the independent variable ξ , from the the elastic wave front ξ_w up to the cavity wall $\xi = 1$, see Fig. 2. The following boundary conditions have been used for the cavity wall:

$$v = 1, \quad \Sigma_{rr} = -P$$

and for the elastic wave front:

$$v = 0, \quad \Sigma_{rr} = \Sigma_{\theta\theta} = 0$$

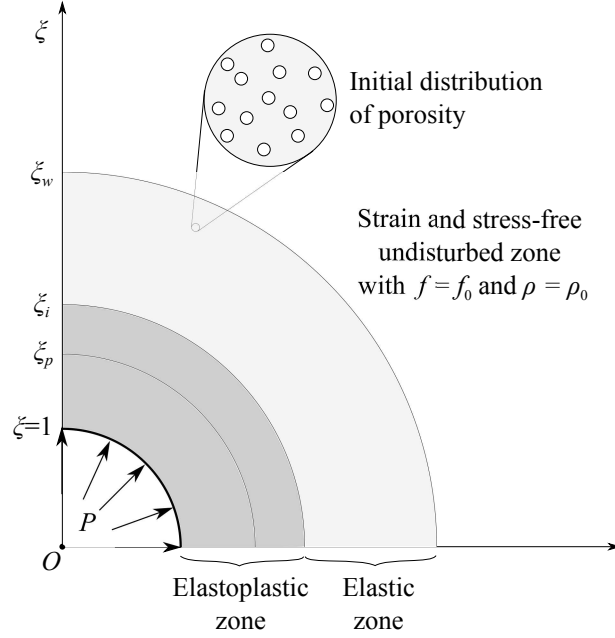


Figure 2: Illustration of the steady cavity expansion field in a porous medium. The dimensionless internal pressure $P = p/E$ is applied at the cavity wall where the dimensionless radial coordinate $\xi = r/a = 1$. The remote region, at $\xi > \xi_w$, is a strain and stress-free undisturbed zone with $f = f_0$ and $\rho = \rho_0$, while behind the elastic wave front, at $\xi = \xi_w$, an elastic range develops. The transition between the elastic and elastoplastic regions is denoted by ξ_i , and the location of the plastic shock wave by ξ_p (a plastic shock wave emerges at high cavitation velocities). This figure is adapted from Durban and Masri (2004).

where $P = p/E$ is the dimensionless applied pressure. The compatibility of the field variables at the interface between the elastic zone and the elastoplastic zone ($\xi = \xi_i$ in Fig. 2) has been enforced using the closed-form elastic solution developed by Durban and Masri (2004). As in Cohen et al. (2010) and Cohen and Durban (2013b), the shooting method is used to determine the unknown coefficient that arises from the elastic solution. The reader is referred to the seminal works of Durban and Masri (2004), Masri and Durban (2005), Cohen et al. (2010) and Cohen and Durban (2013b) to obtain further details on the derivation and numerical integration of this theoretical model (with the exception of the artificial viscosity approach to capture the shocks, which is an original contribution of this paper).

5. Results

This section of the paper is split into two parts. In subsection 5.1 we compare theoretical and numerical results for the case in which the porosity is uniformly distributed in the finite element model, which allows to validate the theoretical model in terms of cavitation velocity, stress and density fields, etc. In subsection 5.2 the comparison is carried out for the case in which the porosity is non-uniformly distributed in the finite element model. The goal is to assess the capability of the theoretical model to predict cavitation fields in metallic materials with a microstructure characterized by the random distribution of void nucleating particles (Tvergaard and Needleman,

2006; Srivastava et al., 2014, 2017). As mentioned before, such microstructure is idealized here, using a 2D approach, as initial material porosity (N’souglo and Rodríguez-Martínez, 2018).

5.1. Uniform initial distribution of porosity

Fig. 3 shows the variation in dimensionless applied pressure P with dimensionless cavitation velocity m , see equation (A.25), for three different values of the initial porosity f_0 : 0.001, 0.01 and 0.1. The theoretical and finite element results are compared within a wide range of cavitation velocities $0.04 \leq m \leq 0.35$. The agreement between both approaches is excellent, demonstrating the potential of the theoretical model to determine the $P - m$ relation. For the three values of f_0 investigated, the cavitation velocity increases with the applied pressure, the $P - m$ curve featuring a concave-upward shape, as in Cohen and Durban (2013b). While the difference between the results obtained for $f_0 = 0.001$ and $f_0 = 0.01$ can hardly be noticed, the $P - m$ curve obtained for $f_0 = 0.1$ shows that, for any given applied pressure within the range of values of P explored, the cavitation velocity is greater as the initial porosity increases. The finite element calculations for $f_0 = 0.1$ and $m > 0.2$ were performed using a linear viscosity parameter $\varpi = 0.6$ greater than the default value of ABAQUS/Explicit (2013). This was necessary so that the code could complete the calculations, despite the large gradients of stress, strain and strain rate that develop in these computations. The numerical simulations predict that for $m = 0.04$ the time required to reach the steady-state expansion of the cavity is $\approx 30 - 35 \mu\text{s}$, whereas for $m = 0.35$ is $\approx 2 - 3 \mu\text{s}$, for the three initial porosities investigated. Loading times of the same order of magnitude were reported by Rodríguez-Martínez et al. (2014) for von Mises materials with different strain hardening behaviours. Note that for values of m greater than 0.35, for the largest value of initial porosity considered $f_0 = 0.1$, despite of the artificial damping and the Arbitrary Lagrangian Eulerian adaptive meshing used in the finite element simulations, excessive element distortion was found in some calculations at the cavity wall and within the shock wave. Therefore, we selected $m = 0.35$ as the upper bound for the cavitation velocities investigated.

Fig. 4 shows the dimensionless von Mises flow stress Σ_e (also referred to as effective von Mises stress in section 2 and Appendix A), see equations (A.11)-(A.12), versus the dimensionless radial coordinate ξ for calculations conducted with three different values of initial porosity, $f_0 = 0.001$, 0.01 and 0.1, and two different cavitation velocities, $m = 0.04$ and 0.35. These are the smallest and greatest cavitation velocities investigated. Theoretical and finite element results are compared. Note that the flow stress results correspond to the elastoplastic material response, i.e. they are the solution of the constitutive problem, see Appendix A. In each of the six plots of Fig. 4 we present finite element results for three different loading times for which the steady-state cavitation has been reached: $40 \mu\text{s}$, $50 \mu\text{s}$ and $60 \mu\text{s}$ if the cavitation velocity is $m = 0.04$, and $10 \mu\text{s}$, $20 \mu\text{s}$ and $30 \mu\text{s}$ if $m = 0.35$. In all cases the agreement between theoretical and finite element results is good, which shows that the theoretical model, in conjunction with the artificial viscosity approach, captures the stress fields that develop in the specimen. Note that the finite element results obtained for different loading times *virtually* lie on top of each

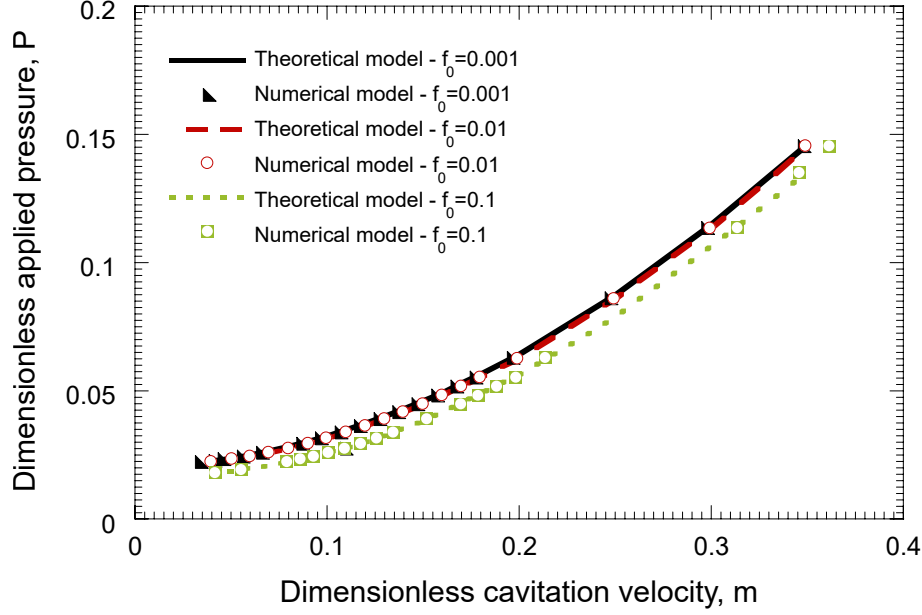


Figure 3: Variation in dimensionless applied pressure P with dimensionless cavitation velocity m for three different values of the initial porosity f_0 : 0.001, 0.01 and 0.1. The theoretical and finite element results are compared. The distribution of initial porosity in the finite element model is uniform.

other, confirming the self-similarity of the cavitation field, as it is assumed in the theoretical model, see section 4. Meaningful differences are only found for the greatest porosity and cavitation velocity analysed, as will be discussed later on. Note that there is an elastic wave –with the front located at ξ_w (elastic precursor)– induced by the application of the velocity/pressure boundary conditions which compresses the material up to the initial elastic limit which is located at ξ_i . This elastic wave is followed by a plastic wave that compresses further the material (Czarnota et al., 2017). As the cavitation velocity increases, the elastoplastic interface becomes closer to the elastic precursor, see Cohen and Durban (2015). Furthermore, it is worth mentioning that, as it has been discussed by Cohen et al. (2010), no jump (shock) conditions are expected in the primary field variables at the elastic precursor. Accordingly, we have not observed an elastic shock in the calculations performed in this work, for the range of cavitation velocities investigated, and the material behavior considered. Next, we carry out specific analyses of the 6 plots presented in Fig. 4.

Figs. 4(a)-(b) show results for $f_0 = 0.001$ –the lowest porosity considered– and the two cavitation velocities investigated. For $m = 0.04$, which corresponds to Fig. 4(a), the $\Sigma_e - \xi$ curve shows a *kink* for $\xi \approx 4.77$ that defines the interface between the elastic zone (on the right) and the elastoplastic zone (on the left). Recall that in section 4 this interface was denoted by ξ_i . The $\Sigma_e - \xi$ curve, both to the right and to the left of the kink, features a concave-upward shape. As expected, the flow stress decreases as we move away from the cavity wall (which corresponds to $\xi = 1$). The values of Σ_e for $\xi = 1$ and ξ_i are ≈ 0.0086 and ≈ 0.0043 , respectively. Note that, according to the asymptotic analysis developed by Durban and Masri (2004), Σ_e should be unbounded at the cavity wall. However, this is not the case for the calculations performed in this work. It seems that, due to

the discretization and the numerical solution of the problem, the flow stress has a finite value at the cavity wall. We have checked that the specific value of Σ_e for $\xi = 1$ depends on the tolerance of the shooting method in the theoretical model, and the size of the elements at the cavity wall in the finite element simulations. Moreover, for $\xi \gtrsim 15$ the value of Σ_e is below 10^{-5} . This radial coordinate defines the elastic wave front. For $m = 0.35$, which corresponds to Fig. 4(b), the $\Sigma_e - \xi$ curve shows a *bump*, a brief speed-up in the decrease of Σ_e followed by a short plateau, which is located just before the elastic / elastoplastic interface $\xi_i \approx 2.51$. Note that the location of the elastic / elastoplastic interface depends on the cavitation velocity (see Fig. 7). The bump, which is zoomed in the upper right part of the plot, indicates the region of the specimen in which the porosity turns from zero for $\xi < 2.19$ to f_0 for $\xi > \xi_i$. Both to the left of the bump and to the right of ξ_i , the $\Sigma_e - \xi$ curve features a concave-upward shape. The value of Σ_e at the cavity wall is ≈ 0.0087 , similar to the case of $m = 0.04$. Note also that the value of Σ_e is below 10^{-5} for $\xi \gtrsim 3.32$. This radial coordinate defines the elastic wave front.

Figs. 4(c)-(d) show results for the initial porosity $f_0 = 0.01$, and the cavitation velocities $m = 0.04$ and $m = 0.35$. For $m = 0.04$, which corresponds to Fig. 4(c), the $\Sigma_e - \xi$ curve is similar to the one obtained for the smaller porosity $f_0 = 0.001$. There is a kink, located at the radial coordinate ≈ 4.67 , which corresponds to the elastic / elastoplastic interface ξ_i . The branches of the $\Sigma_e - \xi$ curve on both sides of the kink also feature a concave-upward shape. In addition, $\Sigma_e \approx 0.0086$ for $\xi = 1$, as in the case of $f_0 = 0.001$. For $m = 0.35$, which corresponds to Fig. 4(d), the bump shown for $f_0 = 0.001$ has turned into a sudden drop of Σ_e —which partially bounces back immediately after—followed by a short plateau. While the end of the plateau, as mentioned before, corresponds to the elastic / elastoplastic interface $\xi_i = 2.36$, the sudden drop of Σ_e indicates the emergence of a shock wave $\xi_p \approx 2.20$, as discussed by Cohen and Durban (2013b). Both in the theoretical model and the finite element simulations, the change in the effective stress induced by the shock, while abrupt, is not a discontinuity, i.e. the shock has a finite width due to the artificial viscosity used in both approaches, see sections 3, 4 and Appendix A. In fact, the drop of Σ_e is less abrupt, i.e. the width of the shock wave is greater, in the finite element simulations than in the theoretical model (see the zoom in the upper right part of the figure). We have checked that, in all the finite element simulations, the element size is smaller than the width of the shock, i.e. there are at least two elements within the shock. The fact that the effective stress is non-monotonic in the shock region (it drops and partially bounces back immediately after) occurs due to the porosity of the material and the small strain hardening considered, see Table 1. We have checked that this effect is reduced increasing the strain hardening, and seems to vanish if the initial porosity is zero (fully dense material). The material does not unload in the shock wave, we have checked in the finite element simulations that the plastic strain in the material increases monotonically with time. Moreover, we have also checked in our calculations that both circumferential and radial stresses decrease monotonically with ξ . Nevertheless, these results are not shown in this paper for the sake of brevity.

Figs. 4(e)-(f) show results for $m = 0.04$ and $m = 0.35$, and the greatest initial porosity investigated $f_0 = 0.1$. For $m = 0.04$, the kink of the $\Sigma_e - \xi$ curve, in comparison with the cases $f_0 = 0.001$ and $f_0 = 0.01$, is shifted leftwards $\xi_i = 3.90$ (see Fig. 7). To the right of the kink, the $\Sigma_e - \xi$ curve features a concave-upward shape, as for the smaller initial porosities considered. However, as we move to the left of the kink, the $\Sigma_e - \xi$ curve first shows a sort of plateau and after a rapid increase in Σ_e . In fact, near the cavity, the gradients of flow stress are greater than for $f_0 = 0.001$ and $f_0 = 0.01$. For $m = 0.35$, which corresponds to Fig. 4(f), the abrupt change in Σ_e that indicates the emergence of a shock is more pronounced than for $f_0 = 0.01$, see Fig. 4(d). The flow stress drops from ≈ 0.0065 to ≈ 0.0023 for $\xi_p \approx 1.70$, immediately bounces back until ≈ 0.0033 , and then increases moderately until reaching a peak which corresponds to the elastic / elastoplastic interface $\xi_i \approx 1.81$. Recall that the finite element calculation reported in Fig. 4(f) has been performed using a value of the linear viscosity parameter $\varpi = 0.6$ greater than the default value of ABAQUS/Explicit (2013), see section 3. It was necessary to increase the viscosity so that the code could complete the calculation. Moreover, note that the values of ξ_p and ξ_i are smaller as the cavitation velocity and the material porosity increase, as it will be discussed later on.

Fig. 5 shows, for the theoretical model, the elastoplastic flow stress Σ_e (denoted simply as flow stress in Figs. 4 and 9), the viscous flow stress Σ^v and the total flow stress $\bar{\Sigma} = \Sigma_e + \Sigma^v$, see equations (A.22) and (A.29), versus the dimensionless radial coordinate ξ for $m = 0.35$ and $f_0 = 0.01$ (as Fig. 4(d)). The $\Sigma_e - \xi$ and $\bar{\Sigma} - \xi$ curves are very similar. The ratio Σ^v/Σ_e is $\approx 3\%$ at the cavity wall and decreases with ξ until the shock wave location is reached. The emergence of the shock leads to a sharp increase of Σ^v that leads to a peak of $\bar{\Sigma}$. For values of the radial coordinate greater than ξ_p the value of Σ^v drops rapidly and the ratio Σ^v/Σ_e becomes smaller than 1% .

Fig. 6 shows the dimensionless material density ρ/ρ_0 , see equation (A.21), versus the dimensionless radial coordinate ξ for the same initial porosities and cavitation velocities that were reported in Fig. 4. The results of the theoretical model and the numerical simulations are compared, and satisfactory agreement is found between both approaches. Meaningful differences are only found for the greatest porosity and cavitation velocity investigated, as it will be discussed later on. For the lowest porosity considered $f_0 = 0.001$, Figs. 6(a)-(b), the density decreases smoothly as we move away from the cavity wall, for both cavitation velocities investigated. The theoretical model predicts that, at the cavity wall, $\rho/\rho_0 \approx 1.02$ for $m = 0.04$, and ≈ 1.18 for $m = 0.35$. Slightly greater values are predicted by the finite element model. Note that, according to the asymptotic analysis developed by Durban and Masri (2004), the hydrostatic stress should be unbounded at the cavity wall, and consequently the density should drop to zero. However, this is not the case for the calculations performed in this work, most likely, due to the discretization and numerical solution of the problem (as mentioned before). We have checked that the specific value of the density for $\xi = 1$ depends on the tolerance of the shooting method in the theoretical model, and

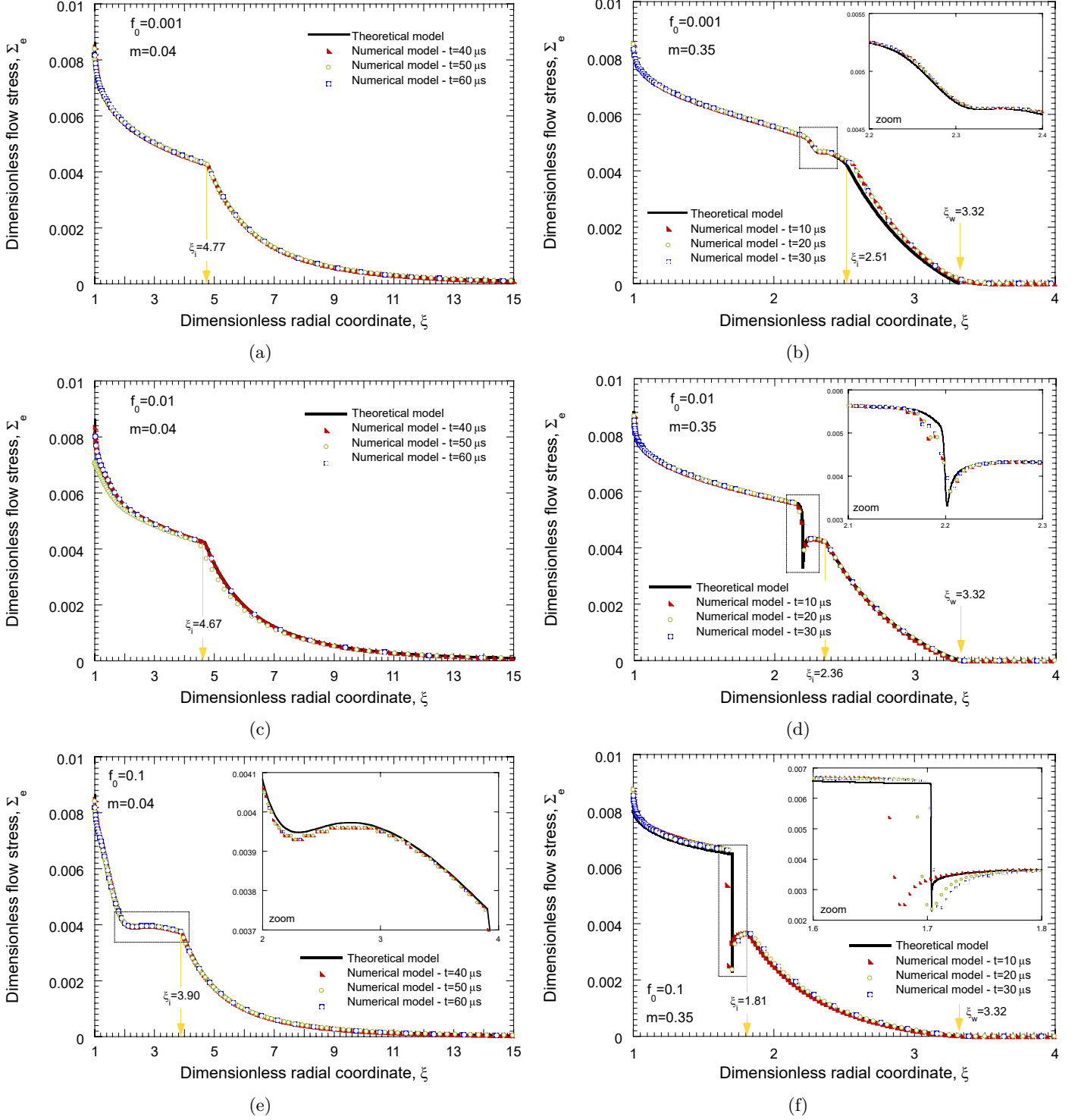


Figure 4: Dimensionless flow stress Σ_e versus dimensionless radial coordinate ξ . Comparison between the theoretical model and finite element results obtained for different loading times. Three different values of the initial porosity f_0 and two different cavitation velocities m are considered: (a) $f_0 = 0.001$ and $m = 0.04$, (b) $f_0 = 0.001$ and $m = 0.35$, (c) $f_0 = 0.01$ and $m = 0.04$, (d) $f_0 = 0.01$ and $m = 0.35$, (e) $f_0 = 0.1$ and $m = 0.04$, (f) $f_0 = 0.1$ and $m = 0.35$. The distribution of initial porosity in the finite element model is uniform.

the size of the elements at the cavity wall in the finite element simulations. For the intermediate initial porosity $f_0 = 0.01$, and the cavitation velocity $m = 0.04$, the ratio ρ/ρ_0 reaches ≈ 1.03 for $\xi = 1$, and it decreases smoothly

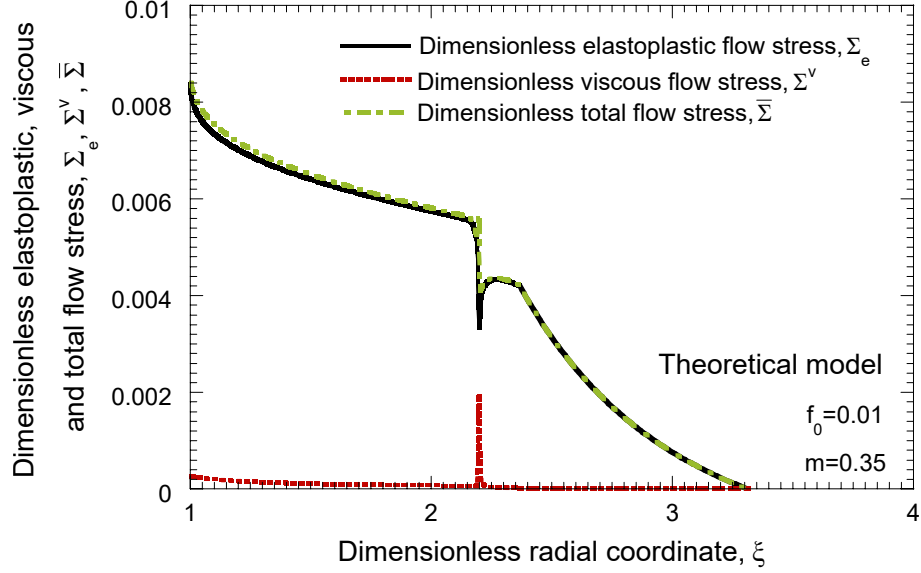


Figure 5: Theoretical model results. Elastoplastic flow stress Σ_e (denoted simply as flow stress in Figs. 4 and 9), viscous flow stress Σ^v and total flow stress $\bar{\Sigma} = \Sigma_e + \Sigma^v$ versus dimensionless radial coordinate ξ . The cavitation velocity is $m = 0.35$ and the initial porosity is $f_0 = 0.01$.

as we move away from the cavity wall, see Fig. 6(c). However, for the same initial porosity and higher cavitation velocity $m = 0.35$, the ratio ρ/ρ_0 shows an abrupt drop which corresponds to the shock wave. Note that the drop of ρ/ρ_0 in Fig. 6(d) and the drop of Σ_e in Fig. 4(d) occur for the same value of the radial coordinate. Moreover, the zoom in the upper right part of Fig. 6(d) shows that the drop in density while abrupt, is not a discontinuity. As mentioned before, this is due to the artificial viscosity included in the theoretical model and the finite element simulations. The results for the greater initial porosity investigated are shown in Figs. 6(e)-(f). For the cavitation velocity $m = 0.04$ the density decreases smoothly with the radial coordinate. However, for $m = 0.35$, the ratio ρ/ρ_0 drops from 1.185 to 1.007 for a value of the radial coordinate ≈ 1.70 due to the emergence of a shock wave (i.e. $\xi_p \approx 1.70$), as discussed in Fig. 4(f). Moreover, note that the finite element results for different times do not lie on top of each other. For $\xi < \xi_p$, the numerical results for $10 \mu s$ are above the numerical results for $20 \mu s$ and $30 \mu s$ and these, in turn, are slightly above the theoretical results. Recall that in this finite element simulation we increased the value of the linear viscosity parameter ϖ from 0.06 to 0.6.

Fig. 7 shows the variation in the locations of the elastic / elastoplastic interface ξ_i and the shock wave ξ_p with the dimensionless cavitation velocity m for two different values of the initial porosity, $f_0 = 0.01$ and $f_0 = 0.1$. The theoretical and finite element results are compared, and very good agreement is found between the results obtained with both approaches. The results for $f_0 = 0.001$ are not shown because no shocks were found for this level of porosity for the range of cavitation velocities analysed in this paper. In fact, we have checked that for $f_0 = 0.001$ shocks emerge for values of m greater than ≈ 0.43 . On the other hand, for 0.01 and 0.1 the minimum values of m for which shock waves appear are 0.26 and 0.14, respectively. The location of the shock wave is taken,

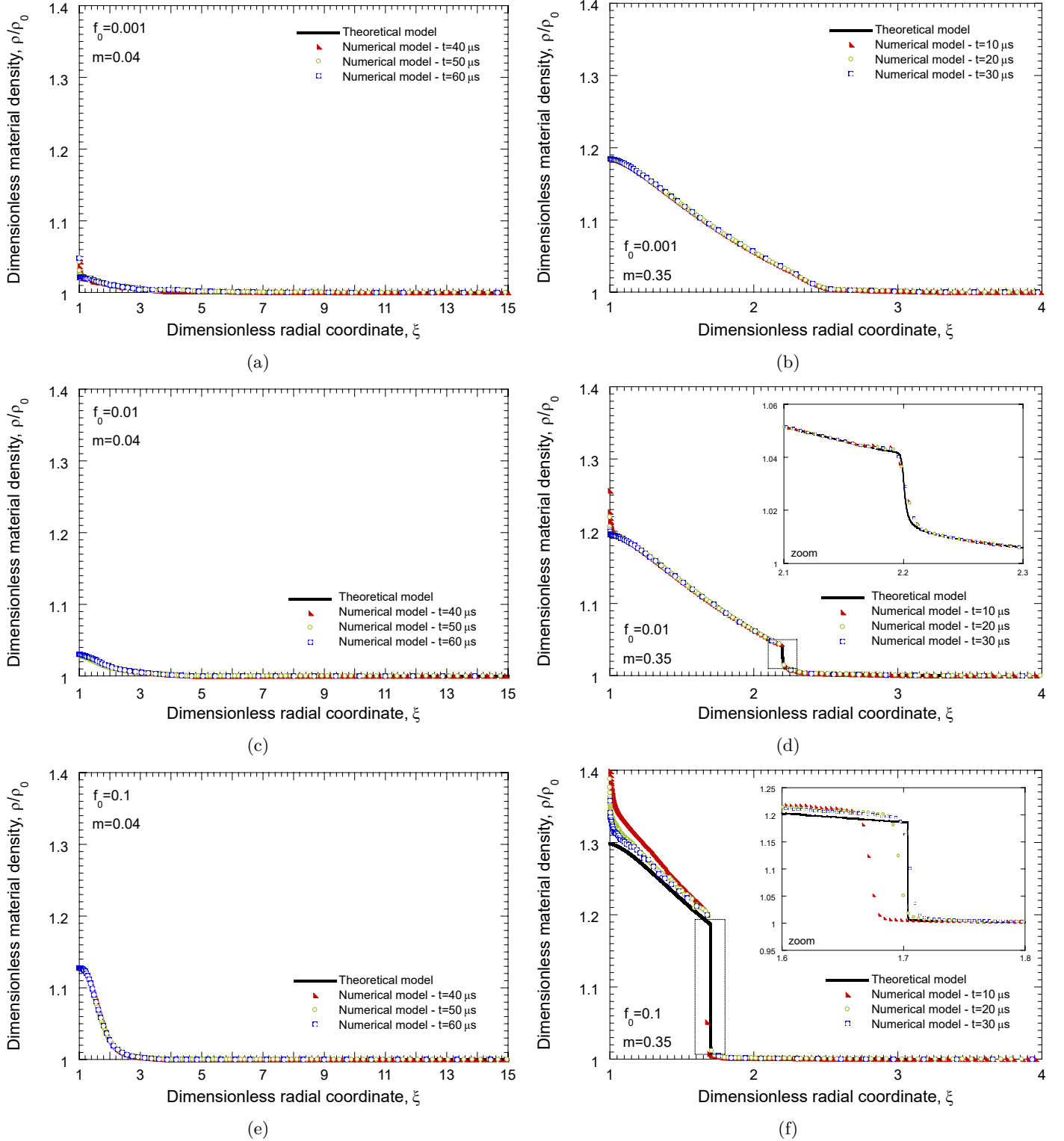


Figure 6: Dimensionless material density ρ/ρ_0 versus dimensionless radial coordinate ξ . Comparison between the theoretical model and finite element results obtained for different loading times. Three different values of the initial porosity f_0 and two different cavitation velocities m are considered: (a) $f_0 = 0.001$ and $m = 0.04$, (b) $f_0 = 0.001$ and $m = 0.35$, (c) $f_0 = 0.01$ and $m = 0.04$, (d) $f_0 = 0.01$ and $m = 0.35$, (e) $f_0 = 0.1$ and $m = 0.04$, (f) $f_0 = 0.1$ and $m = 0.35$. The distribution of initial porosity in the finite element model is uniform.

both in the theoretical model and the finite element simulations, as the radial coordinate for which $v' \leq -1.4$, where $v' = dv/d\xi$, see equation (A.1). On the other hand, the location of the elastic / elastoplastic interface is taken as the minimum radial coordinate for which the plastic strains are zero. Note that ξ_i and ξ_p decrease with m for both values of f_0 considered, i.e. the elastic / elastoplastic interface and the shock wave are closer to the cavity wall as the cavitation velocity (i.e. the applied pressure) increases. Note also that, for a given initial porosity, the values of ξ_i and ξ_p get closer to each other as m increases. This observation agrees with the theoretical results reported by Cohen et al. (2010) who claimed that increasing m will eventually lead to $\xi_i = \xi_p$. In addition to favouring the emergence of shocks at lower cavitation velocities, the increase in porosity also brings closer to the cavity wall the elastic / elastoplastic interface and the shock wave. Note that the $\xi_i - m$ and $\xi_p - m$ curves for $f_0 = 0.1$ are below the curves for $f_0 = 0.01$, being the gap between curves of different porosities rather constant for the whole range of cavitation velocities considered. Recall that for the initial porosity $f_0 = 0.1$, the finite element calculations for $m > 0.2$ are performed using the increased linear viscosity parameter $\varpi = 0.6$.

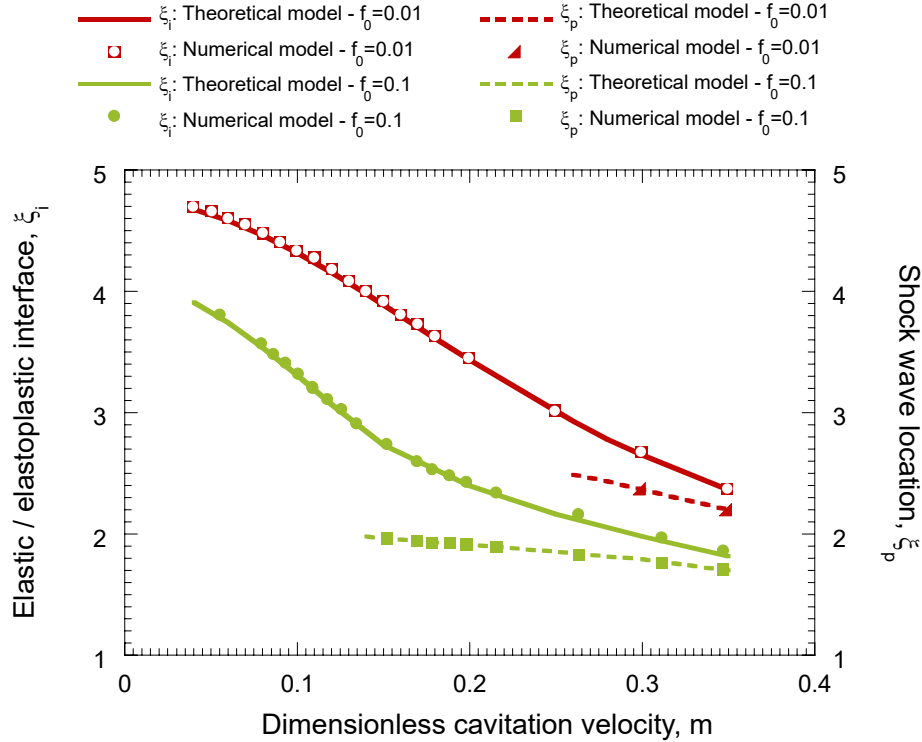


Figure 7: Variation in the locations of elastic / elastoplastic interface ξ_i and shock wave ξ_p with dimensionless cavitation velocity m for two different values of the initial porosity, $f_0 = 0.01$ and $f_0 = 0.1$. The theoretical and finite element results are compared. The distribution of porosity in the finite element calculations is uniform.

To be noted that the results presented in Figs. 4, 6 and Fig. 7 confirm the theoretical predictions of Cohen and Durban (2013b): shock waves emerge in dynamic spherical cavitation fields in Gurson materials, and their intensity increases with the cavitation velocity and the initial material porosity. These theoretical predictions are

validated in this paper using finite element simulations. On the other hand, it has to be noted that Cohen and Durban (2015) showed that for planar shocks, except for small porosities ($f_0 < 0.001$), the porosity delays the appearance of plastic shock waves. Therefore, it becomes apparent that the influence of material porosity on the emergence of shock waves depends on the specific problem addressed (geometry, boundary conditions, stress state, etc.). Further research is still needed to elucidate the specific mechanisms which control the role of porosity on the emergence of shock waves in elastoplastic porous media.

5.2. Non-uniform initial distribution of porosity

Firstly, we check whether the cavitation velocity in specimens which include non-uniform distributions of porosity matches with the one obtained in samples with the porosity homogeneously distributed in the bulk (those presented in previous section). For that purpose, Fig. 8 shows the radial velocity of a node located at the cavity wall \dot{a} versus the loading time t for finite element simulations with specimens in which the porosity is uniformly and non-uniformly distributed in the material. The node taken for the velocity measurements was identified in Fig. 1. The results in Fig. 8 correspond to the initial porosity $f_0 = 0.01$ and the cavitation velocity $m = 0.35$. Recall that for this combination of f_0 and m , shock waves are formed in the sample, see section 5.1. Recall also that in the simulations with non-uniform distributions of porosity the value of f_0 is the average porosity in the specimen, see section 3.1. Results are shown for different non-uniform distributions of porosity in which the percentage of nodes that do have initial porosity is $F = 10\%$, 25% or 40% , and the relative standard deviation of the distribution is $C_v = 5\%$, 15% or 25% . Note that the $\dot{a} - t$ curves obtained from the simulations with uniform and non-uniform distributions of porosity are very similar. The steady-state cavity expansion (i.e. $\dot{a} = \text{constant}$) starts at $t \approx 2 - 3 \mu\text{s}$, as mentioned in section 5.1, and the velocity of the cavity is $\dot{a} \approx 1060 \text{ m/s}$, which corresponds to $m \approx 0.35$. On the other hand, note that for the simulations which consider a non-uniform distribution of porosity the radial velocity \dot{a} shows slight fluctuations which are more accentuated as the value of C_v increases and the value of F decreases, i.e. as the porosity distribution becomes *more heterogeneous*. Note that for the values of F and C_v considered, the variation of F has greater impact on the fluctuations of the $\dot{a} - t$ curves than the variation of C_v . On the other hand, note that we have checked that similar results to those presented in Fig. 8 are obtained for other combinations of f_0 and m .

Secondly, we check whether the cavitation fields in the samples with non-uniform distribution of porosity are self-similar. For that purpose, Fig. 9 shows the dimensionless flow stress Σ_e versus the dimensionless radial coordinate ξ for calculations conducted with $f_0 = 0.01$, and two cavitation velocities, $m = 0.04$ and $m = 0.35$. The theoretical results are compared with finite element results corresponding to different loading times. In the finite element calculations the flow stress is measured along the *radial path 1* identified in Fig. 1. The numerical calculations correspond to a specimen with non-uniform distribution of porosity for which $C_v = 15\%$ and $F = 25\%$. For the smallest cavitation velocity, Fig. 9(a), the three $\Sigma_e - \xi$ curves obtained from the finite element simulations

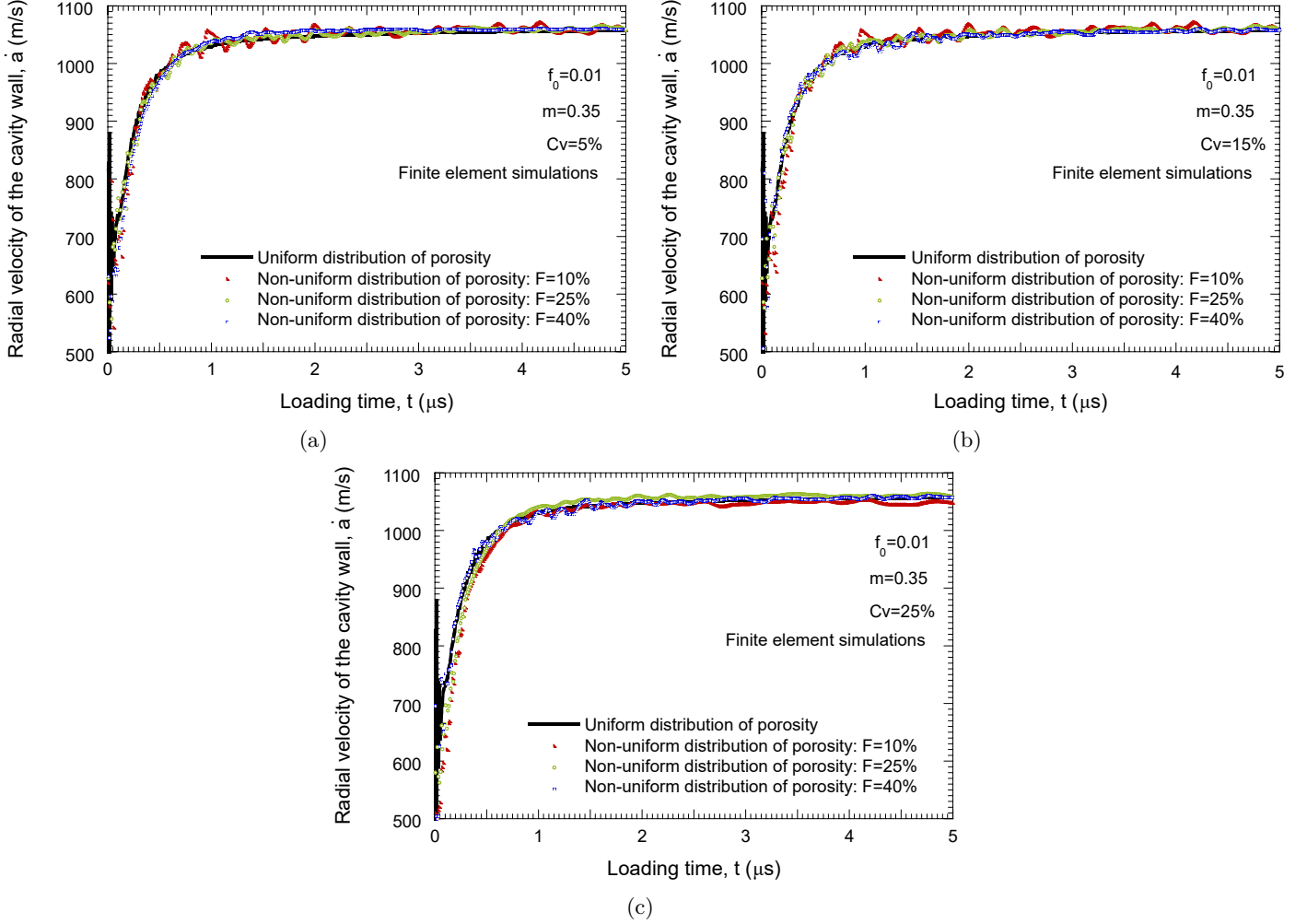


Figure 8: Radial velocity of a node located at the cavity wall \dot{a} versus the loading time t for finite element simulations in which the porosity is uniformly and non-uniformly distributed in the material. The initial porosity and the cavitation velocity are $f_0 = 0.01$ and $m = 0.35$. Results are shown for different non-uniform distributions of porosity in which the percentage of nodes that do have initial porosity is $F = 10\%$, 25% or 40% , and the relative standard deviation is: (a) $C_v = 5\%$, (b) $C_v = 15\%$ and (c) $C_v = 25\%$.

are very similar to the theoretical one. There are some slight fluctuations of the flow stress, i.e. deviations from the theoretical solution, only for values of ξ smaller than ξ_i (the porosity does not affect the elastic range). For this cavitation velocity, the influence of the non-uniform distribution of porosity on the flow stress field is small. On the other hand, for the greatest cavitation velocity, Fig. 9(b), the non-uniformity in the porosity distribution plays a greater role in the numerical results. Note in the zoom shown in the upper right part of the plot that the gradients of flow stress within the shock wave vary with the loading time. Note also the fluctuations of the flow stress for values of ξ slightly smaller than ξ_p . Nevertheless, we have checked that the theoretical predictions find satisfactory agreement with the numerical $\Sigma_e - \xi$ curves for any combination of f_0 , C_v and F studied in this paper. The self-similarity of the cavitation fields, for the specimens with non-uniform distribution of porosity, is further illustrated in Fig. 10 which shows the dimensionless material density ρ/ρ_0 versus the dimensionless radial coordinate ξ for the same calculations of Fig. 9. The theoretical model is compared with finite element results

obtained for different loading times. In the finite element calculations, the material density is measured along the *radial path 1* identified in Fig. 1. For $m = 0.04$, Fig. 10(a), the numerical results show oscillations in the density, which are more accentuated as we approach the cavity wall. The zoom in the upper right part of the figure shows that these oscillations are dependent on the loading time considered. On the other hand, leaving these oscillations aside, the three finite element curves are similar to each other, and they are also similar to the theoretical curve. For $m = 0.35$, Fig. 10(b), the analysis is very much alike. On the one hand, there are fluctuations of the density which are more important close to the cavity wall. On the other hand, the three finite element curves and the analytical curve are similar, i.e. the average slope of the $\rho/\rho_0 - \xi$ curve before the shock wave is similar, the location of the shock wave is also the same, etc. Comparable agreement between theoretical and numerical predictions for the density fields has been found for any other combination of f_0 , C_v and F considered in this paper.

The results presented in Figs. 9 and 10 show that, while there is an influence of the porosity distribution on the numerical results, the cavitation fields in specimens with the non-uniform distributions of porosity used in this paper can be considered self-similar. In addition, it is shown that the theoretical model presented in section 4 provides a good estimation of the cavitation fields that develop in these specimens.

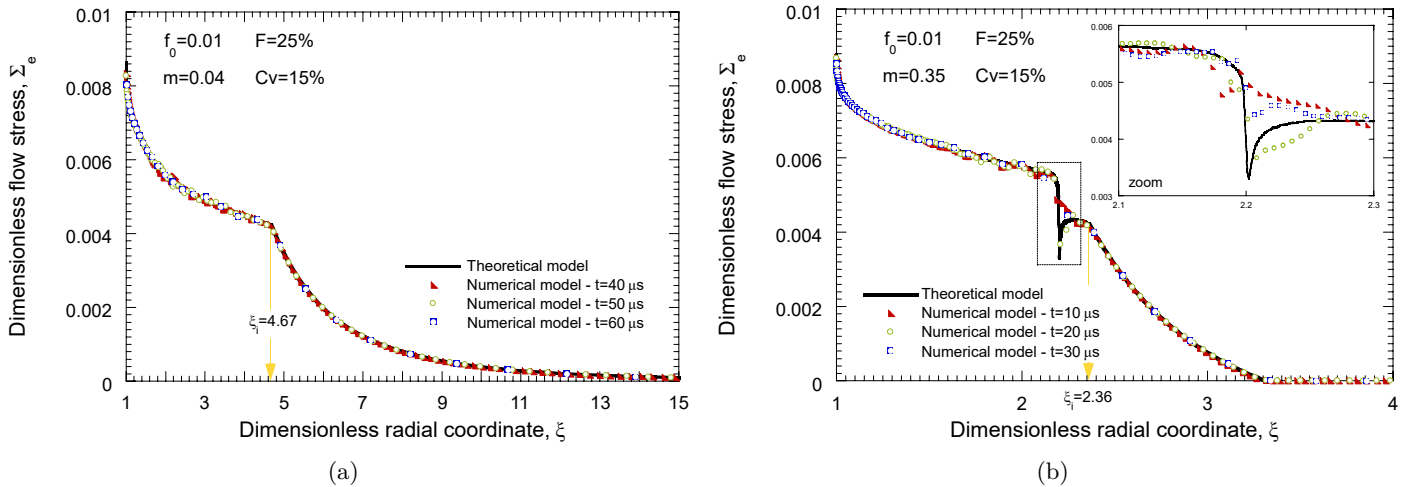


Figure 9: Dimensionless flow stress Σ_e versus dimensionless radial coordinate ξ for *radial path 1* (see Fig. 1). Comparison between the theoretical model and finite element results obtained for different loading times. The numerical calculations correspond to a specimen with non-uniform distribution of porosity for which $C_v = 15\%$ and $F = 25\%$. The initial material porosity is $f_0 = 0.01$. The cavitation velocity is: (a) $m = 0.04$ and (b) $m = 0.35$.

The finite element contours of material density ρ and effective plastic strain rate $\dot{\epsilon}^p$ in specimens with uniform and non-uniform distributions of porosity are shown in Figs. 11 and 12, respectively. The cavitation velocity is $m = 0.35$, the loading time $t = 20 \mu s$, and the initial porosity $f_0 = 0.01$. For the specimen with non-uniform distribution of porosity we have that $C_v = 15\%$ and $F = 25\%$, as in Figs. 9 and 10. Note that the contours of material density ρ and effective plastic strain rate $\dot{\epsilon}^p$ are shown in a plane that contains the center of the sphere (this plane has been obtained by sweeping from 0° to 180° the axisymmetric model built in ABAQUS).

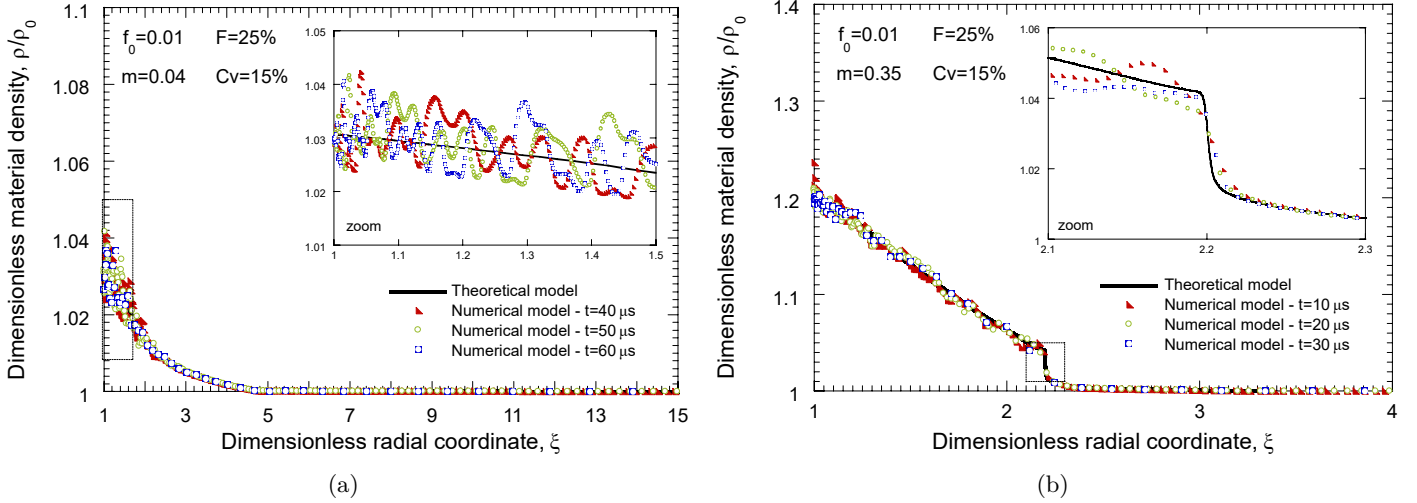


Figure 10: Dimensionless material density ρ/ρ_0 versus dimensionless radial coordinate ξ for *radial path 1* (see Fig. 1). Comparison between the theoretical model and finite element results obtained for different loading times. The numerical calculations correspond to a specimen with non-uniform distribution of porosity for which $C_v = 15\%$ and $F = 25\%$. The initial material porosity is $f_0 = 0.01$. The cavitation velocity is: (a) $m = 0.04$ and (b) $m = 0.35$.

The colour coding in Fig. 11 is such that values of material density ranging from 7600 kg/m^3 (the initial value) to 9000 kg/m^3 correlate with a colour scale that goes from blue to red. If the value of the material density is above 9000 kg/m^3 , it remains red. No values of ρ below 7600 kg/m^3 were obtained. The contours of Fig. 11 show that the material density fluctuates along the circumferential direction in the specimen for which the distribution of porosity is non-uniform (unlike what occurs in the sample with uniform initial porosity). In addition, the non-uniformity of the initial porosity distribution makes density not to decrease monotonically with the radial coordinate (as it was also shown in Fig. 10), i.e. the color scale is not traversed unidirectionally from top to bottom as we move away from the cavity wall. For instance, in the specimen with non-uniform distribution of porosity, along any radial path, there are *yellow elements* (or green, or light blue) closer to the cavity than *red elements* (or yellow, or green). Note that this is not the case for the specimen with uniform distribution of porosity. Note also that the transition from light blue to dark blue, which is very well defined in the density contours for both specimens, corresponds to the shock wave.

The colour coding in Fig. 12 is such that effective plastic strain rates ranging from 10^3 s^{-1} to 10^5 s^{-1} correlate with a colour scale that goes from blue to red. Effective plastic strain rates below 10^3 s^{-1} remain blue and above 10^5 s^{-1} remain red. The contour plots show an outer ring, located at some distance from the cavity wall, in which the plastic strain rate reaches its maximum value. This outer ring, whose width varies between $\approx 300 \text{ }\mu\text{m}$ and $\approx 700 \text{ }\mu\text{m}$, is the shock wave. Similar shocks widths were reported in the recent work of Czarnota et al. (2017) for metallic porous materials. Depending on the loading time, there may be from 2 to more than 10 elements inside the shock (recall that the element size varies with the radial coordinate). The evolution of the effective plastic strain rate with the radial coordinate for the finite element simulations of Fig. 12 is shown in Fig. 13.

The effective plastic strain rate is measured along the *radial path 1*. The value of $\dot{\epsilon}^p$ first decreases as we move away from the cavity wall, then suddenly increases within the shock wave, and the decreases again eventually dropping to zero at the elastic / elastoplastic interface. The maximum effective plastic strain rate, i.e. the shock wave, is located at $\xi_p = 2.20$. The distribution of porosity affects the value of the maximum strain rate attained, which is $\approx 5.2 \cdot 10^5 \text{ s}^{-1}$ for the specimen with uniform distribution of porosity, and $\approx 2.6 \cdot 10^5 \text{ s}^{-1}$ for the specimen with non-uniform distribution of porosity. Similar values (the same order of magnitude) for the maximum strain rate attained in a shock in a porous material were found by Czarnota et al. (2017). While for the specific radial path selected to obtain the finite element results presented in Fig. 13 (*radial path 1*) the inhomogeneous porosity distribution reduces the peak of strain rate, we have checked that for other radial paths, porosity distributions, and loading times, the opposite effect can be obtained. Note also that, outside the shock wave, the strain rate profiles for the specimens with uniform and non-uniform distributions of porosity are very similar.

The influence of the porosity distribution on the strain rate field is further illustrated in Fig. 14, which shows finite element results for specimens with two different porosity distributions for which the relative standard deviation C_v is 15%, and the percentage of nodes with non-zero porosity F is 10% in Fig. 14(a), and 25% in Fig. 14(b). The initial material porosity, cavitation velocity and loading time are $f_0 = 0.01$, $m = 0.35$ and $t = 20 \mu\text{s}$, respectively. The two plots of Fig. 14 show the evolution of $\dot{\epsilon}^p$ with ξ for the two radial paths indicated in Fig. 1: *radial path 1* and *radial path 2*. The strain rate attained in the shock wave is smaller for the *radial path 1*. In addition, the difference between the strain rate attained in the shock wave for the *radial paths 1* and *2* varies with F . This suggests that the *intensity* of the shock wave –assuming that the intensity of the shock wave can be defined by the maximum strain rate– depends on both the average porosity of the specimen and the local porosity at the location of the shock.

6. Summary and concluding remarks

In this paper we have studied dynamic spherical cavitation fields in porous metals with uniform and non-uniform distributions of porosity. For that purpose we have developed a theoretical model and performed finite element simulations in ABAQUS/Explicit (2013). The problem addressed is that of a very large sphere, whose mechanical response is described with the GTN constitutive model, with a small cavity in its center subjected to internal pressure. The theoretical model, based on the seminal work of Cohen and Durban (2013b), has the novelty of using the artificial viscosity approach developed by Wilkins (1980) and Lew et al. (2001) to capture the shock waves that emerge at high cavitation velocities. This is a simple alternative to the methodology used by Cohen et al. (2010) and Cohen and Durban (2013b) who imposed Hugoniot conditions at the shock wave front to obtain the cavitation fields. Note that the artificial viscosity approach used in this paper can also be applied to model

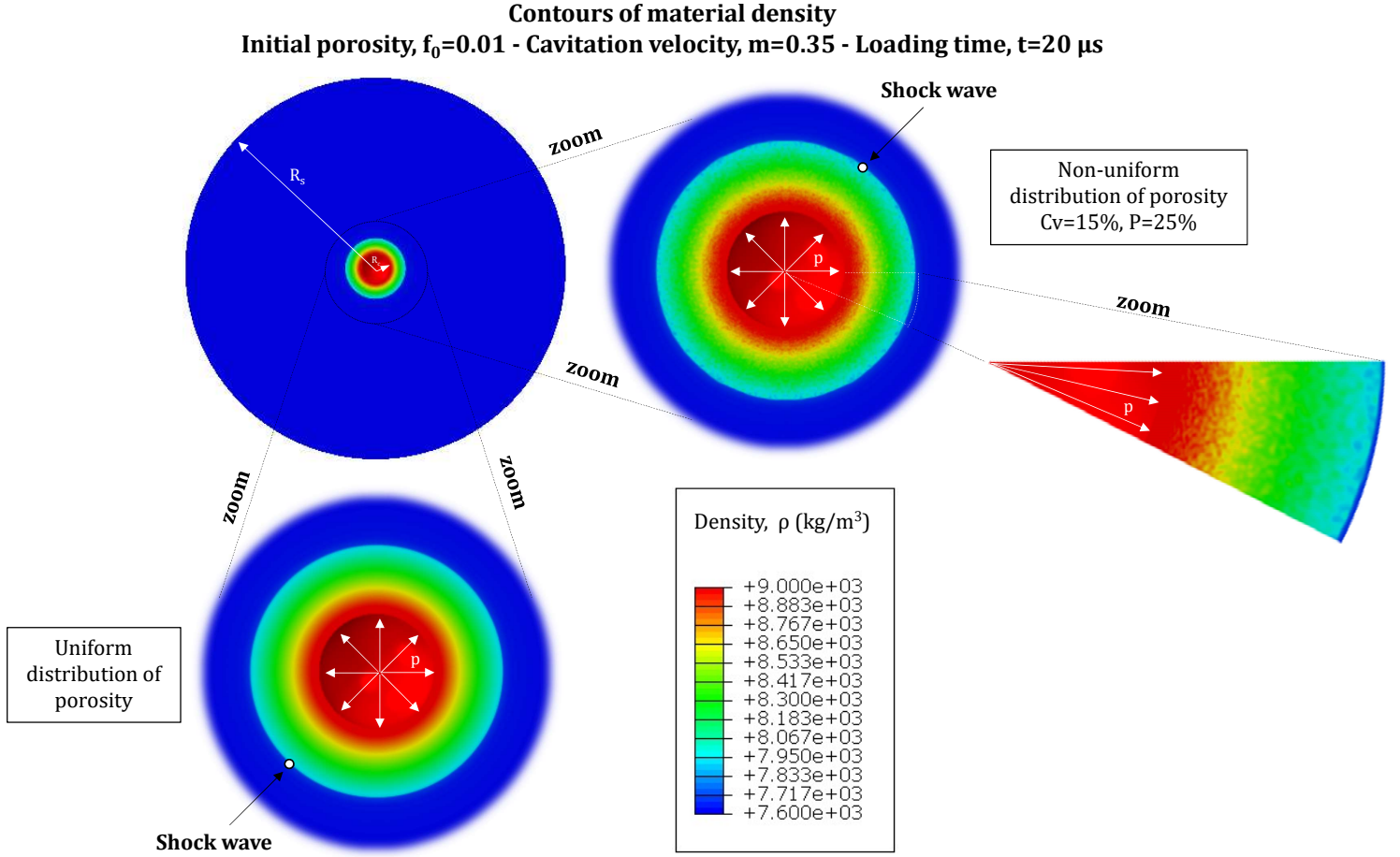


Figure 11: Finite element results. Contours of material density ρ for specimens with uniform and non-uniform distributions of porosity. For the latter case, the values of the distribution parameters are $C_v = 15\%$ and $F = 25\%$. The initial material porosity, cavitation velocity and loading time are $f_0 = 0.01$, $m = 0.35$ and $t = 20 \mu s$, respectively. (For interpretation of the references to colour in the text, the reader is referred to the web version of this article.)

the emergence of shock waves in strain hardening materials with different mechanical behaviours (e.g. anisotropic materials, tension-compression asymmetric materials, etc.) In contrast, for non-hardening materials (even for phase transforming materials with non-hardening phases) further investigations have to be carried out. It has to be noted that ABAQUS/Explicit (2013) also generates bulk viscosity pressures which attenuate the numerical solution and help to model the shock waves. While the theoretical model considers that the initial porosity is uniformly distributed in the material, the finite element model has been used to simulate the cavitation process in specimens with uniform and non-uniform distributions of porosity. The non-uniform distributions of porosity, that aim at idealizing the micro-structure of metallic materials with inclusions and second-phase particles randomly distributed in the bulk, are generated using the methodology developed by N'souglo and Rodríguez-Martínez (2018) which assigns positive values of initial porosity to some nodes and zero to the others. The theoretical

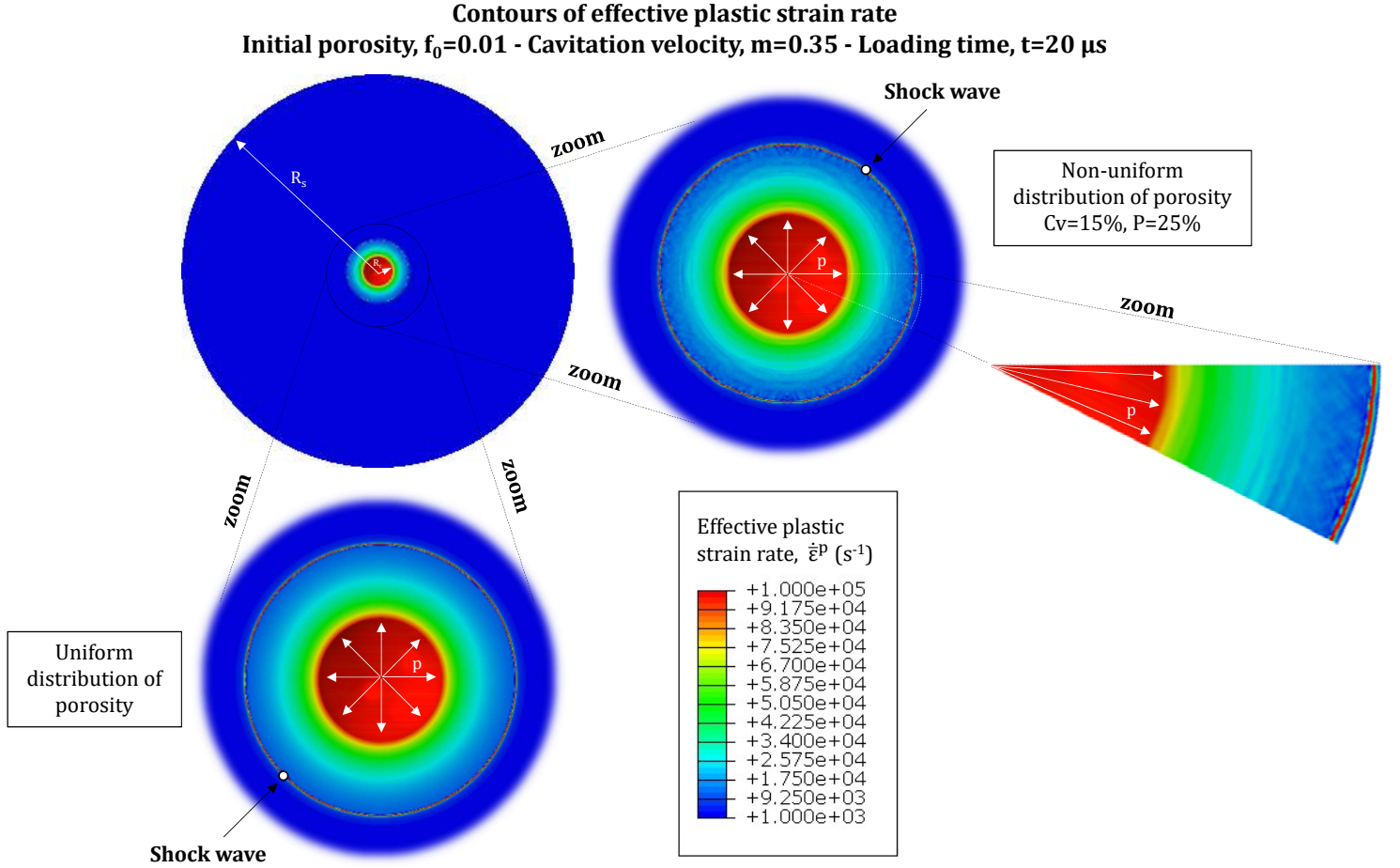


Figure 12: Finite element results. Contours of effective plastic strain rate $\dot{\epsilon}^P$ for specimens with uniform and non-uniform distributions of porosity. For the latter case, the values of the distribution parameters are $C_v = 15\%$ and $F = 25\%$. The initial material porosity, cavitation velocity and loading time are $f_0 = 0.01$, $m = 0.35$ and $t = 20 \mu s$, respectively. (For interpretation of the references to colour in the text, the reader is referred to the web version of this article.)

model and the finite element calculations yielded the following results:

- Uniform distribution of porosity: the theoretical model predicts cavitation velocities in agreement with the finite element calculations for the three values of initial porosity investigated: $f_0 = 0.001$, 0.01 and 0.1 . Both theoretical and finite element model show that the increase of porosity and applied pressure leads to higher cavitation velocities. Moreover, the finite element simulations predict that the time required to reach the steady-state limit turns from $30 - 35 \mu s$ for the lowest cavitation velocity investigated ($m = 0.04$), to $2 - 3 \mu s$ for the highest ($m = 0.35$). Note also that the finite element calculations confirm the self-similarity of the cavitation fields, as it is assumed in the theoretical model. Furthermore, it has been shown that the porosity favours the development of shock waves in the spherical cavity expansion problem, which confirms the theoretical predictions of Cohen and Durban (2013b). Namely, the first shock appears for $m = 0.26$

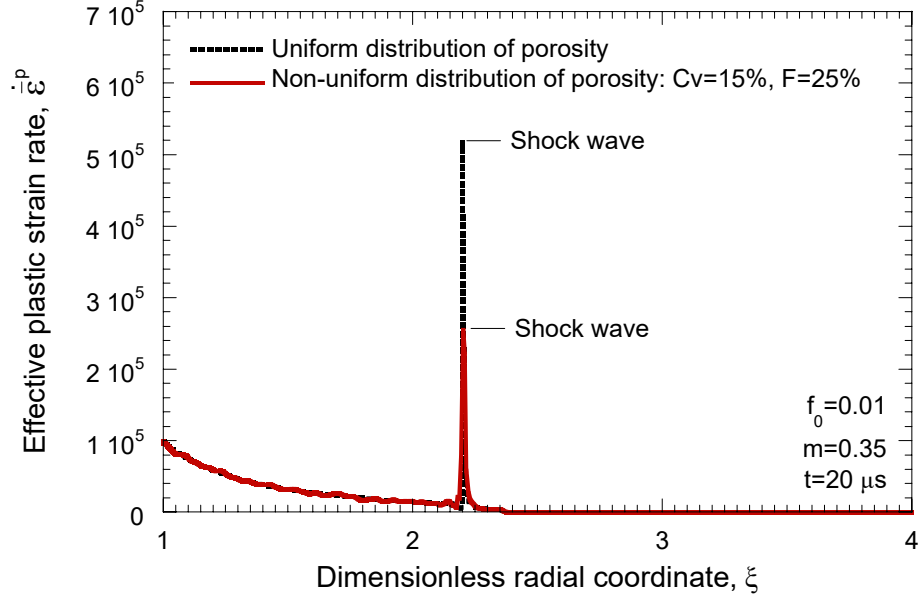


Figure 13: Effective plastic strain rate $\dot{\epsilon}^p$ versus dimensionless radial coordinate ξ for *radial path 1* (see Fig. 1). Finite element results for specimens with uniform and non-uniform distributions of porosity. For the latter case, the values of the distribution parameters are $C_v = 15\%$ and $F = 25\%$. The initial material porosity, cavitation velocity and loading time are $f_0 = 0.01$, $m = 0.35$ and $t = 20 \mu s$, respectively.

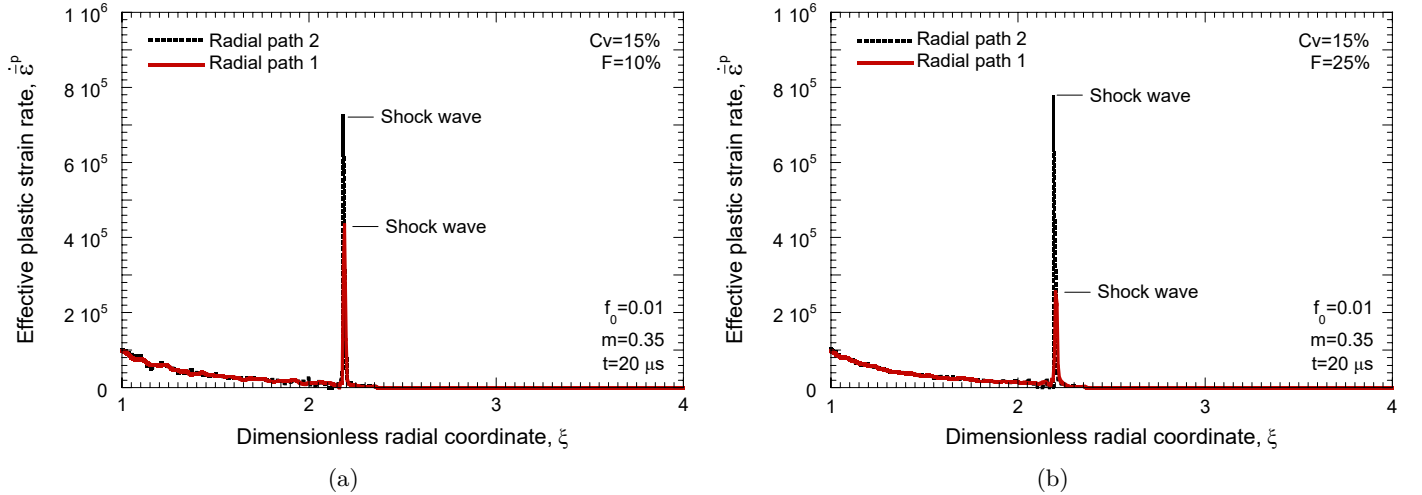


Figure 14: Effective plastic strain rate $\dot{\epsilon}^p$ versus dimensionless radial coordinate ξ for *radial paths 1 and 2* (see Fig. 1). Finite element results for specimens with two different porosity distributions: (a) $C_v = 15\%$ and $F = 10\%$ and (b) $C_v = 15\%$ and $F = 25\%$. The initial material porosity, cavitation velocity and loading time are $f_0 = 0.01$, $m = 0.35$ and $t = 20 \mu s$, respectively.

if the initial porosity is $f_0 = 0.01$, and for $m = 0.14$ if $f_0 = 0.1$. For the initial porosity $f_0 = 0.001$ no shock emerges for the cavitation velocities investigated. Moreover, both theoretical and finite element model predict that the shock wave is located closer to the cavity wall as the cavitation velocity and the initial porosity in the material increase. It has also been shown that, while cavitation velocity and initial porosity boost the intensity of the shock wave, both theoretical and the finite element model do not predict a discontinuity in the field variables for the values of f_0 and m investigated. Due to the artificial viscosity included in the theoretical model and the finite element calculations the shock has a finite width that, in

the finite element simulations, for the combinations combination of f_0 and m investigated, ranges between 300 μm and 700 μm .

- Non-uniform distribution of porosity: the finite element simulations have shown that the cavitation velocity and the time to reach the steady-state limit in specimens which include uniform and non-uniform distributions of porosity is very similar. However, for the specimens with non-uniform distributions of porosity the time evolution of the radial velocity of the cavity wall shows fluctuations which are more accentuated as the number of nodes in the specimen with initial porosity F decreases, and the relative standard deviation of the porosity distribution C_v increases. The finite element simulations also predict fluctuations in the flow stress and density fields which are more important as F decreases and C_v increases. Leaving these fluctuations aside, which depend on the loading time and are particularly important near the cavity wall, the flow stress and density fields in the samples with non-uniform distributions of porosity are shown to be self-similar. In fact, there is general agreement between the results of the theoretical model for the flow stress and density fields, and the average response of the sample predicted by the finite element calculations. This is a key outcome which suggests that the theoretical model can also be used to predict dynamic cavitation fields in materials with inhomogeneous microstructures characterized by the random distribution of defects such as voids or second phase particles. The limitation of the theoretical model lies in the prediction of the intensity of the shock in such materials since it is dependent on the local porosity at the shock location, as shown by the strain rate profiles obtained from the finite element simulations. Outside the shock wave, the cavitation response seems to be mainly controlled by the average properties of the material.

In summary, the theoretical model proposed in this work, which is a modification of the original formulation reported in the seminal paper of Cohen and Durban (2013b), captures the main features of the elastoplastic fields induced by a pressurized spherical cavity expanding dynamically in porous metallic specimens modelled using the Gurson-Tvergaard-Needleman approach. Only for the specimens with non-uniform distributions of porosity it is necessary a full numerical solution to describe the shock wave that emerges at high cavitation velocities, since its intensity depends on the local material porosity. The combined numerical and theoretical approach developed here should be enriched in future works including micro-inertia effects that, at high strain rates, play an important role in the structure of steady shock waves in porous metals (Czarnota et al., 2017).

Acknowledgements

The research leading to these results has received funding from the European Research Council (ERC) under the European Union's Horizon 2020 research and innovation programme. Project PURPOSE, grant agreement 758056.

The authors acknowledge the comments and suggestions of Dr. Tal Cohen (Massachusetts Institute of Technology).

Appendix A. Derivation of the theoretical model

As mentioned in section 4, the core of the theoretical model used in this paper was developed by Cohen and Durban (2013b). The original contributions of the present work are: (1) consider the parameters q_1 and q_2 in the flow potential of the constitutive model, and (2) use an artificial viscosity approach to capture the formation of plastic shocks at high cavitation velocities. The main steps of the model derivation are presented below.

The derivative with respect to the radial coordinate takes the form:

$$\frac{d(\cdot)}{dr} = \frac{d(\cdot)}{d\xi} \frac{d\xi}{dr} = (\cdot)' \frac{1}{a} \quad (\text{A.1})$$

where the prime superscript denotes differentiation with respect to ξ . In addition, as shown by Durban and Fleck (1997), the time derivative is transformed by the similarity relation:

$$\dot{(\cdot)} = \frac{d(\cdot)}{d\xi} \dot{\xi} = (\cdot)' \frac{\dot{a}}{a} (v - \xi) \quad (\text{A.2})$$

where $v = \dot{r}/\dot{a}$ is the dimensionless radial velocity. Note that, in steady-state expansion, \dot{a} is a constant, which leads to $\dot{v} = \ddot{r}/\dot{a}$.

Under spherical expansion conditions, the active components of the strain rate tensor are:

$$d_{rr} = \frac{d\dot{r}}{dr} = \frac{\dot{a}}{a} v' \quad (\text{A.3})$$

$$d_{\theta\theta} = d_{\phi\phi} = \frac{\dot{r}}{r} = \frac{\dot{a}}{a} \frac{v}{\xi} \quad (\text{A.4})$$

where equations (A.1) and (A.2) have been used. Similarly, under spherical expansion conditions, σ_{rr} and $\sigma_{\theta\theta} = \sigma_{\phi\phi}$ are the only active components of the Cauchy stress tensor.

The hypo-elastic law introduced in equation (5) can be rewritten as:

$$\mathbf{d}^e = \frac{1+\nu}{E} \dot{\boldsymbol{\sigma}} - \frac{\nu}{E} \dot{\boldsymbol{\sigma}} : \mathbf{1} \quad (\text{A.5})$$

Note that, in absence of material spin, the objective derivative $\overset{\nabla}{\boldsymbol{\sigma}}$ (see equation (5)) has been replaced by a time derivative $\dot{\boldsymbol{\sigma}}$.

The flow rule introduced in equation (7), using the work conjugacy relation (8), can be rewritten as:

$$\mathbf{d}^p = (1 - f) \frac{\sigma_y \dot{\bar{\varepsilon}}^p}{\boldsymbol{\sigma} : \mathbf{N}} \mathbf{N} \quad (\text{A.6})$$

where the second order tensor \mathbf{N} is:

$$\mathbf{N} = 3 \frac{\mathbf{s}}{\sigma_y^2} + \frac{q_1 q_2 f}{\sigma_y} \sinh \left(\frac{3}{2} \frac{q_2 \sigma_h}{\sigma_y} \right) \mathbf{1} \quad (\text{A.7})$$

Therefore, based on the expressions for the strain rates given in (A.3) and (A.4), the additive decomposition of the rate of deformation tensor, see equation (4), leads to the following two expressions for the radial and circumferential directions:

$$v' = (v - \xi) \left[\Sigma'_{rr} - 2\nu \Sigma'_{\theta\theta} + (1 - f) \frac{\partial \bar{\varepsilon}^p}{\partial \Sigma_y} \Sigma'_y \tilde{N}_{rr} \right] \quad (\text{A.8})$$

$$\frac{v}{\xi} = (v - \xi) \left[-\nu \Sigma'_{rr} + (1 - \nu) \Sigma'_{\theta\theta} + (1 - f) \frac{\partial \bar{\varepsilon}^p}{\partial \Sigma_y} \Sigma'_y \tilde{N}_{\theta\theta} \right] \quad (\text{A.9})$$

where equations (A.1) and (A.2) have been used. Moreover, $\Sigma_{rr} = \sigma_{rr}/E$ and $\Sigma_{\theta\theta} = \sigma_{\theta\theta}/E$ are the dimensionless radial and circumferential stresses. The term $\partial \bar{\varepsilon}^p / \partial \Sigma_y$ is obtained from the definition of the flow strength of the matrix material given in equation (3):

$$\frac{\partial \bar{\varepsilon}^p}{\partial \Sigma_y} = \frac{\varepsilon_0}{n \Sigma_0} \left(\frac{\Sigma_y}{\Sigma_0} \right)^{\frac{1}{n} - 1} \quad (\text{A.10})$$

being $\Sigma_y = \sigma_y/E$ and $\Sigma_0 = \sigma_0/E$ the dimensionless flow strength and the dimensionless initial yield stress of the matrix material, respectively. Moreover, \tilde{N}_{rr} and $\tilde{N}_{\theta\theta}$ are:

$$\tilde{N}_{rr} = \frac{\sigma_y N_{rr}}{\boldsymbol{\sigma} : \mathbf{N}} = -\frac{1}{2} \frac{2 \frac{\Sigma_e}{\Sigma_y} - q_1 q_2 f \sinh \left(\frac{3 q_2}{2} \frac{\Sigma_h}{\Sigma_y} \right)}{\left(\frac{\Sigma_e}{\Sigma_y} \right)^2 + q_1 q_2 f \sinh \left(\frac{3 q_2}{2} \frac{\Sigma_h}{\Sigma_y} \right) \frac{3}{2} \frac{\Sigma_h}{\Sigma_y}} \quad (\text{A.11})$$

$$\tilde{N}_{\theta\theta} = \frac{\sigma_y N_{\theta\theta}}{\boldsymbol{\sigma} : \mathbf{N}} = \frac{1}{2} \frac{\frac{\Sigma_e}{\Sigma_y} + q_1 q_2 f \sinh \left(\frac{3 q_2}{2} \frac{\Sigma_h}{\Sigma_y} \right)}{\left(\frac{\Sigma_e}{\Sigma_y} \right)^2 + q_1 q_2 f \sinh \left(\frac{3 q_2}{2} \frac{\Sigma_h}{\Sigma_y} \right) \frac{3}{2} \frac{\Sigma_h}{\Sigma_y}} \quad (\text{A.12})$$

where $\Sigma_e = \sigma_e/E$ is the dimensionless effective von Mises stress (also referred to as dimensionless flow stress in section 5), $\Sigma_h = \sigma_h/E$ is the dimensionless hydrostatic pressure, and N_{rr} and $N_{\theta\theta}$ are the radial and circumferential

components of the tensor \mathbf{N} , respectively. Note that, under spherical expansion conditions, the dimensionless effective von Mises stress can be expressed as $\Sigma_e = \Sigma_{\theta\theta} - \Sigma_{rr}$.

Moreover, using equations (A.6) and (A.7), the expression for the evolution of the void volume fraction given in (9) can be written as follows:

$$\dot{f} = \frac{3}{2} (1-f)^2 \dot{\varepsilon}^p \frac{q_1 q_2 f \sinh\left(\frac{3}{2} \frac{q_2 \sigma_h}{\sigma_y}\right)}{\left(\frac{\sigma_e}{\sigma_y}\right)^2 + q_1 q_2 f \sinh\left(\frac{3}{2} \frac{q_2 \sigma_h}{\sigma_y}\right) \frac{3}{2} \frac{\sigma_h}{\sigma_y}} \quad (\text{A.13})$$

Using equation (A.2), and the dimensionless stresses Σ_y , Σ_e and Σ_h , previous formula can be rewritten as:

$$f' = \frac{3}{2} (1-f)^2 \frac{q_1 q_2 f \sinh\left(\frac{3q_2}{2} \frac{\Sigma_h}{\Sigma_y}\right)}{\left(\frac{\Sigma_e}{\Sigma_y}\right)^2 + q_1 q_2 f \sinh\left(\frac{3q_2}{2} \frac{\Sigma_h}{\Sigma_y}\right) \frac{3}{2} \frac{\Sigma_h}{\Sigma_y}} \frac{\partial \bar{\varepsilon}^p}{\partial \Sigma_y} \Sigma_y' \quad (\text{A.14})$$

Next, solving the flow potential equation, Eq. (1), for the physical branch of f , it is obtained:

$$f = \frac{1}{q_1} \left[\cosh\left(\frac{3q_2}{2} \frac{\Sigma_h}{\Sigma_y}\right) - \sqrt{\sinh^2\left(\frac{3q_2}{2} \frac{\Sigma_h}{\Sigma_y}\right) + \left(\frac{\Sigma_e}{\Sigma_y}\right)^2} \right] \quad (\text{A.15})$$

Differentiating previous expression with respect to ξ , and inserting the result into equation (A.14), leads to the following expression:

$$\left[q_1 q_2 f \sinh\left(\frac{3q_2}{2} \frac{\Sigma_h}{\Sigma_y}\right) - 2 \frac{\Sigma_e}{\Sigma_y} \right] \Sigma_{rr}' + 2 \left[q_1 q_2 f \sinh\left(\frac{3q_2}{2} \frac{\Sigma_h}{\Sigma_y}\right) + \frac{\Sigma_e}{\Sigma_y} \right] \Sigma_{\theta\theta}' - 2\chi \Sigma_y' = 0 \quad (\text{A.16})$$

with

$$\chi = (1-f)^2 q_1 \left[q_1 f - \cosh\left(\frac{3q_2}{2} \frac{\Sigma_h}{\Sigma_y}\right) \right] \left(\tilde{N}_{rr} + 2\tilde{N}_{\theta\theta} \right) \frac{\partial \bar{\varepsilon}^p}{\partial \Sigma_y} \Sigma_y + \left[q_1 q_2 f \sinh\left(\frac{3q_2}{2} \frac{\Sigma_h}{\Sigma_y}\right) \frac{3}{2} \frac{\Sigma_h}{\Sigma_y} + \frac{\Sigma_e^2}{\Sigma_y^2} \right] \quad (\text{A.17})$$

Moreover, the ratio between current material density ρ and initial material density ρ_0 can be obtained from the balance of mass which, in Eulerian description, takes the form:

$$\dot{\rho} + \rho \text{tr}(\mathbf{l}) = 0 \quad (\text{A.18})$$

where $\mathbf{l} = \mathbf{d}$ in absence of material spin. Thus, equation (A.18), using expressions (A.2), (A.3) and (A.4), leads to:

$$(v - \xi) \frac{\rho'}{\rho} + v' + 2\frac{v}{\xi} = 0 \quad (\text{A.19})$$

Inserting equations (A.8) and (A.9) into the previous expression yields:

$$\frac{\rho'}{\rho} = - \left[3(1 - 2\nu) \Sigma'_h + \frac{f'}{(1 - f)} \right] \quad (\text{A.20})$$

where the definition for f' given in (A.14) has been used.

Integrating equation (A.20) from a given coordinate ξ to the elastic wave front ξ_w , where $f = f_0$, $\rho = \rho_0$, and $\Sigma_h = 0$ (see Fig. 2), a closed-form relation for the density ratio is obtained:

$$\frac{\rho}{\rho_0} = \frac{(1 - f)}{(1 - f_0)} \exp(-3(1 - 2\nu)\Sigma_h) \quad (\text{A.21})$$

Moreover, the balance of linear momentum in the radial direction, in Eulerian description, takes the form:

$$\frac{\partial \bar{\sigma}_{rr}}{\partial r} + \frac{2}{r} (\bar{\sigma}_{rr} - \bar{\sigma}_{\theta\theta}) = \rho \ddot{r} \quad (\text{A.22})$$

where $\bar{\sigma}_{rr}$ and $\bar{\sigma}_{\theta\theta}$ are the *total* radial and circumferential stresses given by the sum of the elastoplastic equilibrium stresses and the viscous stresses, i.e. $\bar{\sigma}_{rr} = \sigma_{rr} + \sigma_{rr}^v$ and $\bar{\sigma}_{\theta\theta} = \sigma_{\theta\theta} + \sigma_{\theta\theta}^v$. While σ_{rr} and $\sigma_{\theta\theta}$ are related to the elastic and plastic deformation rates by means of the constitutive equations, σ_{rr}^v and $\sigma_{\theta\theta}^v$ are related to the total deformation rates by means of an artificial viscosity. In other words, the artificial viscosity approach is only used in the definition of the stresses that enter into the balance of linear momentum.

Following the works of Wilkins (1980) and Lew et al. (2001), the radial and circumferential viscous stresses inserted into equation (A.22) are defined as:

$$\sigma_{rr}^v = \begin{cases} c_0^2 \rho (\Delta r)^2 |d_{rr}| d_{rr} + c_L \rho \Delta r V_s d_{rr} & \text{for } d_{rr} < 0 \\ 0 & \text{for } d_{rr} \geq 0 \end{cases} \quad (\text{A.23})$$

$$\sigma_{\theta\theta}^v = \begin{cases} c_0^2 \rho (\Delta r)^2 |d_{\theta\theta}| d_{\theta\theta} + c_L \rho \Delta r V_s d_{\theta\theta} & \text{for } d_{\theta\theta} < 0 \\ 0 & \text{for } d_{\theta\theta} \geq 0 \end{cases} \quad (\text{A.24})$$

where $c_0 \approx 2$ and $c_L \approx 1$ are constant parameters, Δr is a given increment along the radial direction and $V_s = \sqrt{E/\rho}$. Note that the viscous contribution plays a role only in compression.

Using equation (A.3), the radial viscous stress σ_{rr}^v can be written as:

$$\sigma_{rr}^v = -c_0^2 (\Delta\xi)^2 E \frac{\rho}{\rho_0} m^2 (v')^2 - c_L \Delta\xi E \sqrt{\frac{\rho}{\rho_0}} m |v'| \quad (\text{A.25})$$

where the relations $\dot{a} = m\sqrt{E/\rho_0}$ and $\Delta\xi = \Delta r/a$ have been used. Note that $m = \dot{a}/\sqrt{E/\rho_0}$ is the dimensionless cavitation velocity defined as the ratio between the cavity expansion velocity \dot{a} and the elastic wave velocity in a long rod $\sqrt{E/\rho_0}$.

Using equation (A.4), the circumferential viscous stress can be written as:

$$\sigma_{\theta\theta}^v = -c_0^2 \left(\frac{\Delta\xi}{\xi} \right)^2 E \frac{\rho}{\rho_0} m^2 v^2 - c_L \frac{\Delta\xi}{\xi} E \sqrt{\frac{\rho}{\rho_0}} m |v| \quad (\text{A.26})$$

According to equations (A.25) and (A.26), the dimensionless viscous stresses $\Sigma_{rr}^v = \sigma_{rr}^v/E$ and $\Sigma_{\theta\theta}^v = \sigma_{\theta\theta}^v/E$ become:

$$\Sigma_{rr}^v = - \left(c_0^2 (\Delta\xi)^2 \frac{\rho}{\rho_0} m |v'| + c_L \Delta\xi \sqrt{\frac{\rho}{\rho_0}} m |v'| \right) \quad (\text{A.27})$$

and

$$\Sigma_{\theta\theta}^v = - \left(c_0^2 \left(\frac{\Delta\xi}{\xi} \right)^2 \frac{\rho}{\rho_0} m |v| + c_L \frac{\Delta\xi}{\xi} \sqrt{\frac{\rho}{\rho_0}} m |v| \right) \quad (\text{A.28})$$

Using equations (A.1), (A.2), and relation $m = \dot{a}/\sqrt{E/\rho_0}$, the balance of linear momentum (A.22) can be rewritten in terms of dimensionless stresses as:

$$(\Sigma_{rr} + \Sigma_{rr}^v)' + \frac{2}{\xi} (\Sigma_{rr} - \Sigma_{\theta\theta}) + \frac{2}{\xi} (\Sigma_{rr}^v - \Sigma_{\theta\theta}^v) = m^2 \frac{\rho}{\rho_0} (v - \xi) v' \quad (\text{A.29})$$

References

- ABAQUS/Explicit, 2013. Abaqus Explicit v6.13 User's Manual. version 6.13 ed., ABAQUS Inc., Richmond, USA.
- Aranda-Iglesias, D., Vadillo, G., Rodríguez-Martínez, J.A., 2017. Oscillatory behaviour of compressible hyperelastic shells subjected to dynamic inflation: a numerical study. *Acta Mechanica* 228, 2187–2205.
- Becker, R., 1987. The effect of porosity distribution on ductile fracture. *Journal of the Mechanics and Physics of Solids* 35, 577–599.

- Bilger, N., Auslender, F., Bornert, M., Moulinec, H., Zaoui, A., 2007. Bounds and estimates for the effective yield surface of porous media with a uniform or a nonuniform distribution of voids. *European Journal of Mechanics A/Solids* 26, 810–836.
- Chen, E.P., 1995. Numerical simulation of penetration of aluminum targets by spherical-nose steel rods. *Theoretical and Applied Fracture Mechanics* 22, 159–164.
- Cohen, T., Durban, D., 2013a. Fundamental solutions of cavitation in porous solids: a comparative study. *Acta Mechanica* 224, 1695–1707.
- Cohen, T., Durban, D., 2013b. Hypervelocity cavity expansion in porous elastoplastic solids. *Journal of Applied Mechanics* 80, 011017.
- Cohen, T., Durban, D., 2015. Steady shock waves in porous plastic solids. *International Journal of Solids and Structures* 71, 70–78.
- Cohen, T., Masri, R., Durban, D., 2010. Shock waves in dynamic cavity expansion. *Journal of Applied Mechanics* 77, 041009.
- Czarnota, C., Mercier, S., Molinari, A., 2017. The structure of steady shock waves in porous metals. *Journal of the Mechanics and Physics of Solids* 107, 204–228.
- Durban, D., Fleck, N.A., 1997. Spherical cavity expansion in a Drucker-Prager solid. *Journal of Applied Mechanics* 64, 743–750.
- Durban, D., Masri, R., 2004. Dynamic spherical cavity expansion in a pressure sensitive elastoplastic medium. *International Journal of Solids and Structures* 41, 5697–5716.
- Forrestal, M.J., Brar, N.S., Luk, V.K., 1991. Penetration of strain-hardening targets with rigid spherical-nose rods. *Journal of Applied Mechanics* 58, 7–10.
- Forrestal, M.J., Luk, V.K., 1988. Dynamic spherical cavity-expansion in a compressible elastic-plastic solid. *Journal of Applied Mechanics* 55, 275–279.
- Forrestal, M.J., Luk, V.K., Rosenberg, Z., Brar, N.S., 1992. Penetration of 7075-T651 aluminum targets with ogival-nose rods. *International Journal of Solids and Structures* 29, 1729–1936.
- Forrestal, M.J., Okajima, K., Luk, V.K., 1988. Penetration of 6061-T651 aluminum targets with rigid long rods. *Journal of Applied Mechanics* 55, 755–760.
- Forrestal, M.J., Tzou, D.Y., Askari, E., Longcope, D.B., 1995. Penetration into ductile metal targets with rigid spherical-nose rods. *International Journal of Impact Engineering* 16, 699–710.

- Forrestal, M.J., Warren, T.L., 2008. Penetration equations for ogive-nose rods into aluminum targets. *International Journal of Impact Engineering* 35, 727–730.
- Goodier, J.N., 1965. On the mechanics of indentation and cratering in the solid targets of strain hardening metal by impact of hard and soft spheres. *Proceedings of the 7th symposium on hypervelocity impact*. III, 215–259.
- Gurson, A., 1977. Continuum theory of ductile rupture by void nucleation and growth. Part I: Yield criteria and flow rules for porous ductile media. *ASME Journal of Engineering Materials and Technology* 99, 2–15.
- Hallquist, J.O., 1990. LS-DYNA2D, an explicit two-dimensional hydrodynamic finite element code with interactive rezoning and graphical display. Livermore Software Technology Corporation, Livermore, CA, U.S.A. .
- Hopkins, H.G., 1960. Chapter 3: Dynamic expansion of spherical cavities in metals, in: Sneddon, I.N., Hill, R. (Eds.), *Advances in Applied Mechanics*. New York: North-Holland Publishing Company. volume 1 of *Progress in Solid Mechanics*, pp. 85–164.
- Huang, Y., 1993. The role of nonuniform particle distribution in plastic flow localization. *Mechanics of Materials* 16, 265–279.
- Landshoff, R., 1955. A numerical method for treating fluid flow in the presence of shocks. Technical Report LA-1930. Los Alamos National Laboratory.
- Lew, A., Radovitzky, R., Ortiz, M., 2001. An artificial-viscosity method for the lagrangian analysis of shocks in solids with strength on unstructured, arbitrary-order tetrahedral meshes. *Journal of Computer-Aided Materials Design* 8, 213–231.
- Luk, V.K., Forrestal, M.J., Amos, D., 1991. Dynamic spherical cavity expansion of strain-hardening metals. *Journal of Applied Mechanics* 58, 1–6.
- Masri, R., Durban, D., 2005. Dynamic spherical cavity expansion in an elastoplastic compressible Mises solid. *Journal of Applied Mechanics* 72, 887–898.
- McGlaun, J.M., Thompson, S.L., Elrick, M.G., 1990. CTH: a three-dimensional shock wave physics code. *International Journal of Impact Engineering* 10, 351–360.
- von Neumann, J., Richtmyer, R.D., 1950. A method for the numerical calculation of hydrodynamic shocks. *Journal of Applied Physics* 21, 232–237.
- N’souglo, K.E., Rodríguez-Martínez, J.A., 2018. Non-uniform distributions of initial porosity in metallic materials affect the growth rate of necking instabilities in flat tensile samples subjected to dynamic loading. *Mechanics Research Communications* 91, 87 – 92.

- Ohno, N., Hutchinson, J.W., 1984. Plastic flow localization due to non-uniform void distribution. *Journal of the Mechanics and Physics of Solids* 32, 63–85.
- Rodríguez-Martínez, J.A., Cohen, T., Zaera, R., 2014. Approaching steady cavitation: the time scale in hypervelocity cavity expansion in work hardening and transformation hardening solids. *International Journal of Impact Engineering* 73, 43 – 55.
- Roisman, I.V., Yarin, A.L., Rubin, M.B., 1997. Oblique penetration of a rigid projectile into an elastic-plastic target. *International Journal of Impact Engineering* 19, 769–795.
- Rosenberg, Z., Dekel, E., 2008. A numerical study of the cavity expansion process and its application to long-rod penetration mechanics. *International Journal of Impact Engineering* 35, 147 – 154.
- Rubin, M.B., Kositski, R., Rosenberg, Z., 2016. Essential physics of target inertia in penetration problems missed by cavity expansion models. *International Journal of Impact Engineering* 98, 97–104.
- Srivastava, A., Osovski, S., Needleman, A., 2017. Engineering the crack path by controlling the microstructure. *Journal of the Mechanics and Physics of Solids* 100, 1–20.
- Srivastava, A., Ponson, L., Osovski, S., Bouchaud, E., Tvergaard, V., Needleman, A., 2014. Effect of inclusion density on ductile fracture toughness and roughness. *Journal of the Mechanics and Physics of Solids* 63, 62–79.
- Tvergaard, V., 1981. Influence of voids on shear band instabilities under plane strain conditions. *International Journal of Fracture* 17, 389–407.
- Tvergaard, V., 1982. On localization in ductile materials containing spherical voids. *International Journal of Fracture* 18, 237–252.
- Tvergaard, V., Needleman, A., 1992. Effect of crack meandering on dynamic, ductile fracture. *Journal of the Mechanics and Physics of Solids* 40, 447–471.
- Tvergaard, V., Needleman, A., 2006. Three dimensional microstructural effects on plane strain ductile crack growth. *International Journal of Solids and Structures* 43, 6165–6179.
- Vadillo, G., Zaera, R., Fernández-Sáez, J., 2008. Consistent integration of the constitutive equations of Gurson materials under adiabatic conditions. *Computer Methods in Applied Mechanics and Engineering* 197, 1280–1295.
- Warren, T.L., 2016. The effect of target inertia on the penetration of aluminum targets by rigid ogive-nosed long rods. *International Journal of Impact Engineering* 91, 6–13.
- Warren, T.L., Forrestal, M.J., 1998. Effects of strain hardening and strain rate sensitivity on the penetration of aluminum targets with spherical-nosed rods. *International Journal of Solids and Structures* 35, 3737–3753.

- Wilkins, M.L., 1980. Use of artificial viscosity in multidimensional fluid dynamic calculations. *Journal of Computational Physics* 36, 281 – 303.
- Yarin, A.L., Rubin, M.B., Roisman, I.V., 1995. Penetration of a rigid projectile into an elastic-plastic target of finite thickness. *International Journal of Impact Engineering* 16, 801–831.
- Zhang, Z., 1996. A sensitivity analysis of material parameters for the Gurson constitutive model. *Fatigue & Fracture of Engineering Materials & Structures* 19, 561–570.